Journal of Structural Geology 181 (2024) 105083

Contents lists available at ScienceDirect

Journal of Structural Geology

journal homepage: www.elsevier.com/locate/jsg

Carbonate deformation through the brittle-ductile transition: The case of the SW Helvetic nappes, Switzerland

Giovanni Luca Cardello [a,*], Stefano M. Bernasconi [b], Maria Giuditta Fellin [b], Meinert Rahn [c], Ricarda Rosskopf [b], Colin Maden [b], Neil S. Mancktelow [b]

[a] Department of Chemistry, Physics, Mathematics, and Natural Sciences, Sassari University, Via Piandanna, 4, 07100, Sassari, Italy
[b] Department of Earth Sciences, ETH Zurich, Sonneggstrasse 5, 8092, Zurich, Switzerland
[c] Swiss Federal Nuclear Safety Inspectorate (ENSI), Industriestrasse 19, 5200, Brugg, Switzerland

ARTICLE INFO

Keywords:
Alps
Exhumation
Thermochronology
Stable isotopes
Clumped-isotopes
Fault rocks

ABSTRACT

Carbonate deformation through the brittle-ductile transition (BDT) remains incompletely documented in the field. We therefore investigate the exhumation of the SW-Helvetic nappe stack using a new multi-method approach that integrates optical observations with a revised nomenclature, thermochronology, stable isotopes, and clumped isotope thermometry, aiming to constrain the time-temperature history of BDT deformation processes in carbonates. Single grain (U–Th)/He zircon and apatite fission track ages establish new burial/exhumation trajectories from different nappes, allowing us to infer the thermal history of the Rawil Depression. This prominent doubly-plunging hinge zone between the Mont Blanc and Aar Crystalline Massifs underwent post-nappe faulting, now constrained to the Tortonian-Early Pliocene, reflected in differential exhumation rates of ~0.2 km/Myr between the most depressed area and its easternmost side. Calculating and modelling the rock-buffered clumped isotope temperatures (ranging from ~250 °C to 55 °C), we indirectly date the BDT processes, exemplified by the Rezli Fault. On this structure, possible shear heating during mylonitisation is indirectly dated at 18–15.5 Ma. Progressive embrittlement started around 11–9 Ma at temperatures of about 150–110 °C. Lower clumped isotope temperatures correspond to recent brittle faulting between 9 and 5 Ma. Our results on the regional evolution can be applied to analogous seismogenic carbonate-rich crustal sections.

1. Introduction

Carbonate rocks are widespread in the Alpine-Himalayan belts (Bernoulli and Jenkyns, 1974; Ramsay, 1989; Dürr et al., 2005; Herwegh and Pfiffner, 2005; Pfiffner, 2014) and may be deformed during both burial and exhumation. Along their path to the surface, both temperature and pressure decreased, often leading to strain localization in shear zones and eventually brittle faults (e.g. Sibson, 1977; Handy et al., 2007; Ebert et al., 2007; Doglioni et al., 2015; Passelègue et al., 2019). The transition zone from brittle to viscous (or ductile) behaviour, referred to as the Brittle-Ductile Transition (BDT; cf. Byerlee, 1968; Scholz, 1988) occurs at depths ranging between ca. 5 and 12 km and is the zone where most earthquakes nucleate (e.g., Sibson, 1982; Ranalli and Murphy, 1987). Despite the practical importance, only a few field examples of structural characterisation of carbonates exhumed through the BDT have been carried out in pioneering studies (e.g., Wiederer et al., 2002; Brogi, 2006; Vitale et al., 2007; Tesei et al., 2013; Torgersen and Viola, 2014; Clemenzi et al., 2015; Cardello and Mancktelow, 2015; Zucchi, 2020). The majority of BDT-oriented studies on carbonates have been based on experiments (e.g., Di Toro et al., 2011; Spagnuolo et al., 2015; Nardini et al., 2020). Understanding the microstructural processes related to aseismic and seismic deformation during exhumation of carbonate rocks remains an ongoing challenge (e.g., Delle Piane et al., 2017).

To gain insights into the processes active in carbonates during exhumation through the BDT, we develop a revised structural nomenclature of fault rocks and associated mineralisation, and combine it with 1) zircon and/or apatite low-temperature thermochronology of the host rock and 2) stable and clumped isotope analyses of veined and faulted carbonate rocks, with sampling closely related to the microstructures. This combination provides key constraints on the temperature and origin of the fluids related to different structural processes, the type of fluid-rock interaction and fluid-rock buffering, and on the absolute timing of cooling through a specific temperature range. Low-

* Corresponding author.
E-mail addresses: glcardello@uniss.it, luca.cardello@gmail.com (G.L. Cardello).

https://doi.org/10.1016/j.jsg.2024.105083
Received 14 September 2023; Received in revised form 31 January 2024; Accepted 7 February 2024
Available online 13 February 2024

temperature thermochronological techniques have been widely used to constrain the burial and cooling history of orogens (e.g. Rahn, 2001; Reiners and Brandon, 2006; Fellin et al., 2007). Here, we develop and apply a method for studying deformed carbonates exhumed through the BDT in a case study of the carbonate-rich Helvetic nappe stack in SW Switzerland (Fig. 1), expanding on the results of an earlier PhD thesis (Cardello, 2013) and previous field work (Gasser and Mancktelow, 2010; Cardello and Mancktelow, 2015). The study primarily aims at determining fault and vein formation temperatures within a framework established by the observed relative ages of structures developed during

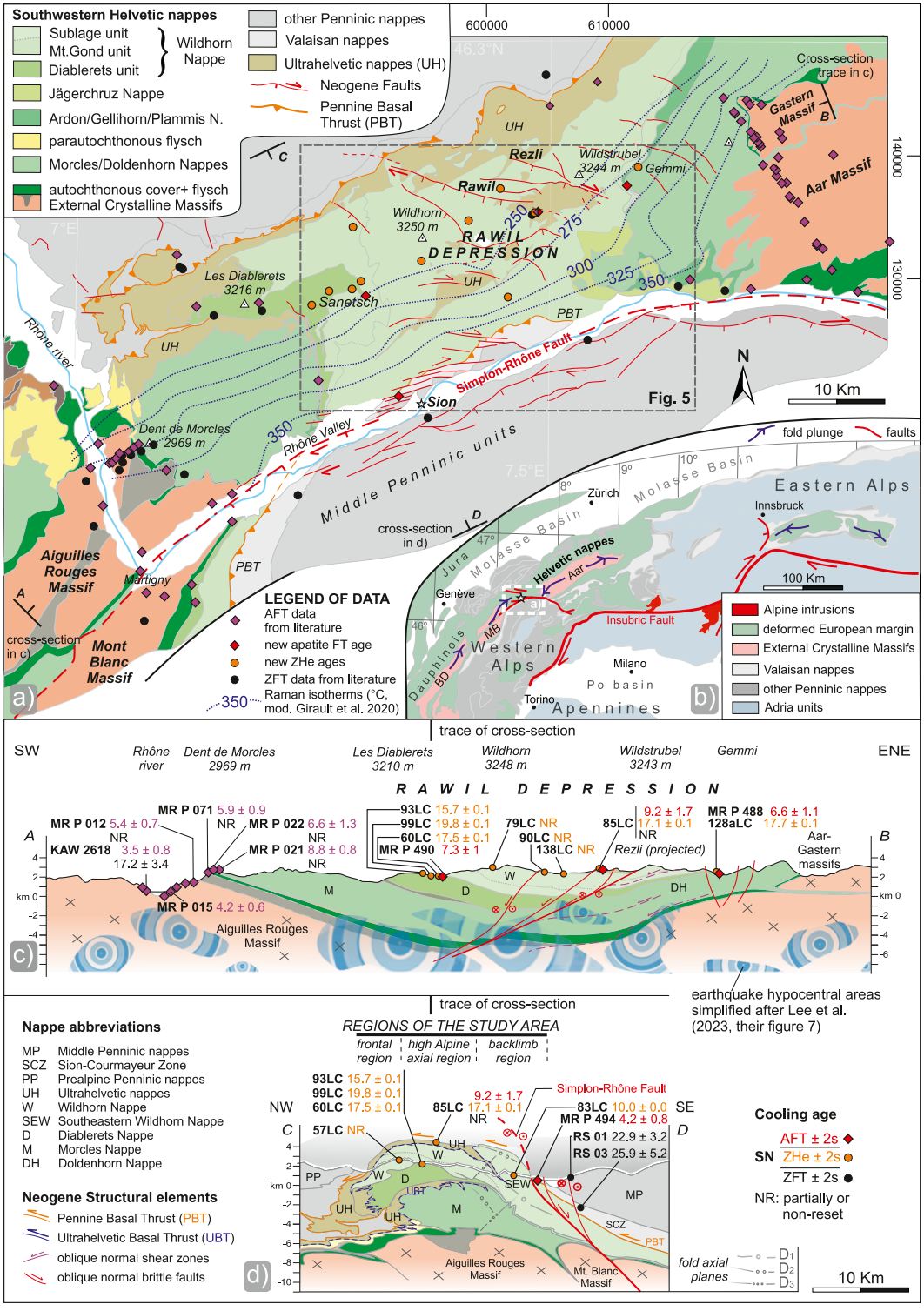

Fig. 1. a) Tectonic sketch map of southwestern Switzerland. Ages from the literature are in black for ZFT, orange for ZHe and violet for AFT (see Table S1). New AFT ages are marked in red. b) Tectonic map of the Alps with location of the study area (white dashed box). c-d) The cross-sections locate available thermochronologic data. The youngest ZHe ages (orange) for each sample are plotted on a profile parallel to the Rawil Depression, c) and perpendicular to it, d) (modified after Cardello et al., 2019). In c), clusters of seismic sources from Lee et al. (2023) are also marked both in the deepest Helvetic nappes and in the crystalline basement. (For interpretation of the references to colour in this figure legend, the reader is referred to the Web version of this article.)

exhumation. In this context, comparing stable isotope data from tectonic structures of different character and relative ages may provide constraints on the source and temperature of the mineralising fluids and of the host rock (e.g., Berio et al., 2022; Tavani et al., 2023). This work also acts as a test study to verify the reliability of clumped isotope temperatures and solid-state bond reordering models between 150 and 250 °C, which represents a common BDT temperature range for carbonates (Burkhard, 1990, 1993; Vitale et al., 2007). These new methods are described in section 3, while the more conventional techniques that were used are described in the Supplementary Material.

In summary, in addition to novel methods, this study aims to (1) establish the regional exhumation history using new (U–Th)/He dating on zircons (ZHe), combined with literature data and new apatite fission track data (AFT), (2) characterise temperatures of vein/fault formation related to the BDT and subsequent brittle structures, and (3) estimate the relative and absolute ages of structures involved in the exhumation.

2. Geological setting

2.1. Tectonic framework

The Bernese Alps (Fig. 1a and b) expose the southwestern part of the Helvetic nappes and consist of a carbonate-rich Triassic to lower Oligocene succession, which recorded the Alpine-Tethyan syn-rift and post-break-up extension of the European crust (e.g., Stampfli et al., 1991; Manatschal et al., 2022). Their stratigraphic architecture reflects the Mesozoic palaeogeography of the European margin: Helvetic platform/ramp, Ultrahelvetic basin and more distal Pennine units (Pfiffner, 2014; Cardello and Mancktelow, 2014; Pantet et al., 2020). Alpine continental collision resulted in nappe stacking of these units (e.g., Dietrich and Casey, 1989; Escher et al., 1993; Pfiffner, 1993). The western Bernese Alps were affected by multiple deformational phases (Fig. 1c and d), the most relevant of which was the overthrust of the Penninic and Ultrahelvetic nappes on top of the Helvetic units, via the Pennine Basal Thrust (PBT) and the Ultrahelvetic Basal Thrust (UBT), respectively (Fig. 1d). In the Penninic nappes, thrusting occurred from ~38 to 19 Ma (Cardello et al., 2019), while thrusting within the Helvetic nappes occurred between 32 and 16 Ma in the highest nappes (such as the Wildhorn Nappe) and between about 27 and 13 Ma in the lowest nappes (Kirschner et al., 2003). The lowest Helvetic nappes (Doldenhorn and Morcles nappes) are attached to their crystalline basement, whereas higher nappes are progressively more allochthonous moving towards the top (e.g. Wildhorn Nappe; Masson et al., 1980; Ramsay et al., 1981). During and after their emplacement, the nappes experienced a transition from ductile to brittle deformation (Dietrich, 1989; Burkhard and Kerrich, 1988; Gasser and Mancktelow, 2010; Cardello and Tesei, 2013; Cardello and Mancktelow, 2015). This was associated with the exhumation of the Mont Blanc-Aiguilles Rouges and Aar-Gastern External Crystalline Massifs (ECMs; Ramsay, 1989; Herwegh et al., 2020; Piantelli et al., 2022).

From north to south (Fig. 1d), three regions can be distinguished in the study area: (1) the 'frontal region' that reached diagenetic metamorphic grade ($T < 220$ °C, Frey and Ferreiro-Mählmann, 1999; Mullis et al., 2017; Girault et al., 2020); (2) the high Alpine 'axial region'; and (3) the southern 'backlimb region' that reached lowermost greenschist facies conditions ($T_{max} = 350 \pm 50$ °C; Coombs et al., 1976; Bussy and Epard, 1984; Herwegh and Pfiffner, 2005). As shown in Fig. 1a, metamorphic zones cross-cut nappe boundaries, reflecting nappe stacking prior to peak metamorphic conditions (Steck, 1984). The axial low of the dome in the nappe stack is known as the Rawil Depression (Heim, 1921, Fig. 1a), which currently preserves the Wildhorn Nappe and several Ultrahelvetic klippen in the 'axial region', whereas in the 'backlimb region' it hosts the Penninic units of the Sion-Courmayeur Zone (SCZ; Trümpy, 1954). The region is crossed by post-nappe faults, the most significant of which, the Simplon-Rhône Fault (Hubbard and Mancktelow, 1992), offsets the whole stack (Fig. 1d). This is associated with: 1) footwall tilt and differential exhumation across the fault (Cardello et al., 2016) and 2) active seismicity (Lee et al., 2023; Truttmann et al., 2023, Fig. 1c), potentially linked to a continuation of the Pleistocene (U–Th ages on fault rocks at Gemmi Pass: 2.5–0.5 Ma), and OSL-dated post-glacial movements interpreted by Ustaszewski et al. (2007) to have occurred within a time range between 8.7 ± 2.0 ka and 2.4 ± 0.5 ka.

2.2. Thermochronologic, geochronologic and stable isotopes studies

Recent studies on the metamorphic grade in the area (Mullis et al., 2017; Berger et al., 2020; Girault et al., 2020; Gnos et al., 2021; Mangenot et al., 2021) constrained the maximum burial temperatures (Fig. 1a). They confirmed that the thermal peak and its corresponding thermal structure within the ECM sedimentary cover were established after thrusting within the Helvetic nappes and persisted for more than 10 Myr, as reported by Boutoux et al., 2016. The interaction between deformation and fluid flow in this region has been the subject of several studies in the 1980s. Dietrich et al. (1983) identified multiple vein sets, whose isotopic composition compared to the host rock indicated a transition from a chemically open to a closed system. Burkhard and Kerrich (1988) subdivided the veins into pre-, syn-, and post-tectonic groups. Their data suggested a closed system within each nappe during their formation, but a more open advective system along the basal thrust of the Doldenhorn Nappe, where fluid migration was considered to be the result of fluid expulsion from the basement. They attributed a late, generally open fluid system to uplift and doming of the ECMs and associated the depleted ^{18}O to the infiltration of meteoric waters to depths of 5–15 km, due to enhanced hydraulic conductivity resulting from fracturing. Better P-T-t constraints on nappe stack development were later provided by Kirschner et al. (1996, 2003) and Cardello et al. (2019), who obtained several ^{40}Ar–^{39}Ar ages on micas from different thrusts to infer their evolution. In particular, Kirschner et al. (1996) determined the thermal history for the Morcles Nappe, which shows rapid burial after sedimentation followed by cooling after 13 Ma to present-day conditions.

In recent decades, several thermochronological studies have quantified the exhumation history of the ECMs in the vicinity of our study area (Fig. 1, e.g. Soom, 1990; Seward and Mancktelow, 1994; Kahle et al., 1997; Reinecker et al., 2008; Campani et al., 2010a, 2010b; Valla et al., 2012, 2016; Fox et al., 2016; Girault et al., 2020; Herwegh et al., 2020). These studies indicate a history of rapid exhumation for the ECMs with distinct age-elevation gradients and AFT ages ranging from 10 to 2 Ma. Exhumation is related to the activity of the Simplon-Rhône Fault (Grasemann and Mancktelow, 1993; Seward and Mancktelow, 1994; Campani et al., 2010a, 2010b; Montemagni and Zanchetta, 2022; Wolff et al., 2024) and during the Pleistocene to alternation between river and glacial erosion, which focused along the Rhône valley (Valla et al., 2012, 2016). However, only a very small amount of AFT and zircon fission track (ZFT) data are available directly from the Helvetic nappes (Fig. 1, Soom, 1990; Rahn, 2001). This limited number of ages was inconclusive as to whether the Rawil Depression was an area of reduced exhumation and/or whether tectonics controlled the exhumation pattern.

3. Materials and methods

3.1. Geological mapping

Sample collection was an integral part of an extensive field mapping campaign. In the 'axial region', this field survey was conducted at 1:10,000 scale over an area of about 200 km^2 (Cardello and Mancktelow, 2014, 2015), while in the 'backlimb region' and the SCZ, an additional ~100 km^2 were mapped at 1:25,000 scale (Fig. 1; Cardello et al., 2019). The stratigraphic subdivision used here follows the nomenclature of the Swiss Commission for Stratigraphy (http://www.stratigraphie.ch).

3.2. Low-temperature thermochronology and thermal modelling

The samples selected for AFT and ZHe dating were collected along a profile traversing the Rawil Depression along the SW-NE Alpine strike (Fig. 1c), and from the backlimb region (Fig. 1d; Table 1). The sampled rocks are from intercalated siliciclastic intervals of the Helvetic succession containing detrital zircons and/or apatites from the Schist Mordorés, Garschella, Wildstrubel, and Taveyannaz Formations and the Ultrahelvetic flysch. The quality and/or quantity of both zircons and apatites were frequently low, significantly restricting the numbers of dateable samples. This limitation precluded the use of the (U–Th)/He method for dating apatites, due to the need for higher quality grains. Analytical methods for both AFT and (U–Th)/He dating as well as for the thermal modelling based on these datasets, are described in the Supplementary Material.

3.3. Structural and microstructural analysis

In order to correlate between regional structures and isotopic data, 109 samples were characterised in terms of location, nappe position, geological formation, geometry and fabric. These samples were categorised into four mesostructural groups: high-angle faults, shear zones, thrusts, and veined rocks. As displayed in Fig. 2a, samples were further classified into macrostructural types on the basis of a revised nomenclature of deformed mineralised rocks, modified after Woodcock and Mort (2008), which for the first time also takes into account veins and brittle-ductile structures.

Detailed microstructural analyses were conducted on 31 polished thin-sections (from 28 hand samples) with an optical microscope, to identify the relationships between the microfabric type and deformation structures and mineral growth. A first macrostructural discrimination divides the samples into: 1) fault rocks *sensu strictu* (i.e. with clasts) characterised by normal to strike-slip or inverse high-angle kinematics; 2) rocks mineralised *in situ* by fluids, including fault mirrors and those with extensional and shear veins. The analysis of the texture of the fault rocks *sensu strictu* took place by studying the fabric of the clasts, the relationship between them, matrix and "healing" cement, and the coherence of the rock, taking into account the presence or absence of an internal foliation. Various macrostructural fabrics could be distinguished, such as

1) Fault breccia: massive fault rock consisting of more than 30% clasts larger than 2 mm;
2) Fault gouge: incoherent fault rock, consisting of less than 30% clasts greater than 2 mm;
3) Calcite-supported massive cataclasite: coherent and massive fault rock, consisting of less than 30% clasts larger than 2 mm, supported predominantly by calcite;
4) Calcite-supported foliated cataclasite: coherent, foliated fault rock with a pervasive internal organisation parallel to the main fault plane consisting of less than 30% clasts greater than 2 mm supported primarily by calcite;

Table 1
Sample locations and lithologies for new ZHe and AFT and clumped-isotope data constrained in this work are presented from west to east.

Sample ID	Locality	Longitude	Latitude	Elev. (m)	Nappe	Rock type	Sedimentary age
Samples for low-temperature thermochronology							
60LC	Tsanfleuron	7.296342	46.323263	2128	Diablerets	Sandstone	Lutetian - Bartonian
MR P 490	Tsanfleuron	7.299915	46.319874	2010	Diablerets	Sandstone	Priabonian *pp.*
93LC	Prarochet	7.262025	46.311070	2423	Diablerets	Sandstone	Priabonian *pp.*
99LC	Viellar	7.278378	46.321143	2209	Diablerets	Sandstone	Priabonian *pp.*
MR P 494	La Muraz (Sion)	7.339864	46.235582	690	Roignais-Versoyen	Calcareous sandstone	Priabonian *pp.*
128aLC	Gemmi	7.602250	46.408765	2497	Doldenhorn	Sandstone	Priabonian - Oligocene *pp*
85LC	Plaine Morte	7.486408	46.370587	2927	Ultrahelvetics	Sandstone	late Eocene - Rupelian
138LC	Rawil	7.457460	46.387498	2479	Wildhorn	Sandstone	early Aptian - early Cenomanian
57LC	Auberge du Sanetsch	7.296627	46.363348	2057	Wildhorn	Sandstone	Priabonian *pp.*
79LC	La Selle	7.370132	46.334297	2726	Wildhorn	Sandstone	Bartonian - Priabonian
90LC	Plan des Roses	7.415584	46.366925	2346	Wildhorn	Sandstone	early Aptian - early Cenomanian
83LC	Bisse du Ro	7.457162	46.312519	1586	Wildhorn	Sandstone	Bajocian
MR P 488	Lämmerenboden	7.581320	46.389857	2535	Gellihorn	Sandstone	Lutetian - Barthonian
Samples for clumped isotopes							
67LC	La Muraz (Sion)	7.33925	46.23561	694	Roignais-Versoyen	Calcitic sigmoid	Triassic (?)
24LC	Les Audannes south	7.39361	46.33581	2459	Wildhorn	Veined limestone	Barremian - Aptian
130LC	Col de l'Arpochey	7.49100	46.35131	2495	Ultrahelvetics	Calcite-supported foliated cataclasite	Oxfordian - Berriasian
84LC	Col du Sé Mort	7.49397	46.37217	2842	Ultrahelvetics	Siliciclastic calcarenite	Oxfordian - Tithonian
113LC	Rezli	7.48426	46.39897	2299	Wildhorn	Mylonitic lens	Barremian - Aptian
114a,bLC	Rezli	7.49693	46.40112	2270	Wildhorn	Matrix-supported massive cataclasite	Barremian - Aptian
RF1	Rezli	7.49749	46.40127	2258	Wildhorn	S/C veined marl	Valanginian – Hauterivian
RF2	Rezli	7.49741	46.40125	2257	Wildhorn	Calcite-supported foliated cataclasite	Valanginian – Hauterivian
RF3	Rezli	7.49736	46.40119	2261	Wildhorn	Cataclasised mylonite	Valanginian – Hauterivian
RF4	Rezli	7.49750	46.40110	2262	Wildhorn	Matrix-supported foliated cataclasite	Valanginian – Hauterivian
RF5	Rezli	7.49779	46.40094	2260	Wildhorn	Matrix-supported massive cataclasite	Valanginian – Hauterivian
RF7	Rezli	7.49781	46.40080	2263	Wildhorn	Mylonitised cataclasite	Barremian - Aptian
129LC	Gemmi Pass	7.60614	46.39687	2270	Doldenhorn	Calcite-supported massive cataclasite	Oxfordian - Berriasian
125LC	Rote Chumme (Gemmi region)	7.61419	46.41771	2278	Doldenhorn	Calcite-supported massive cataclasite	Valanginian

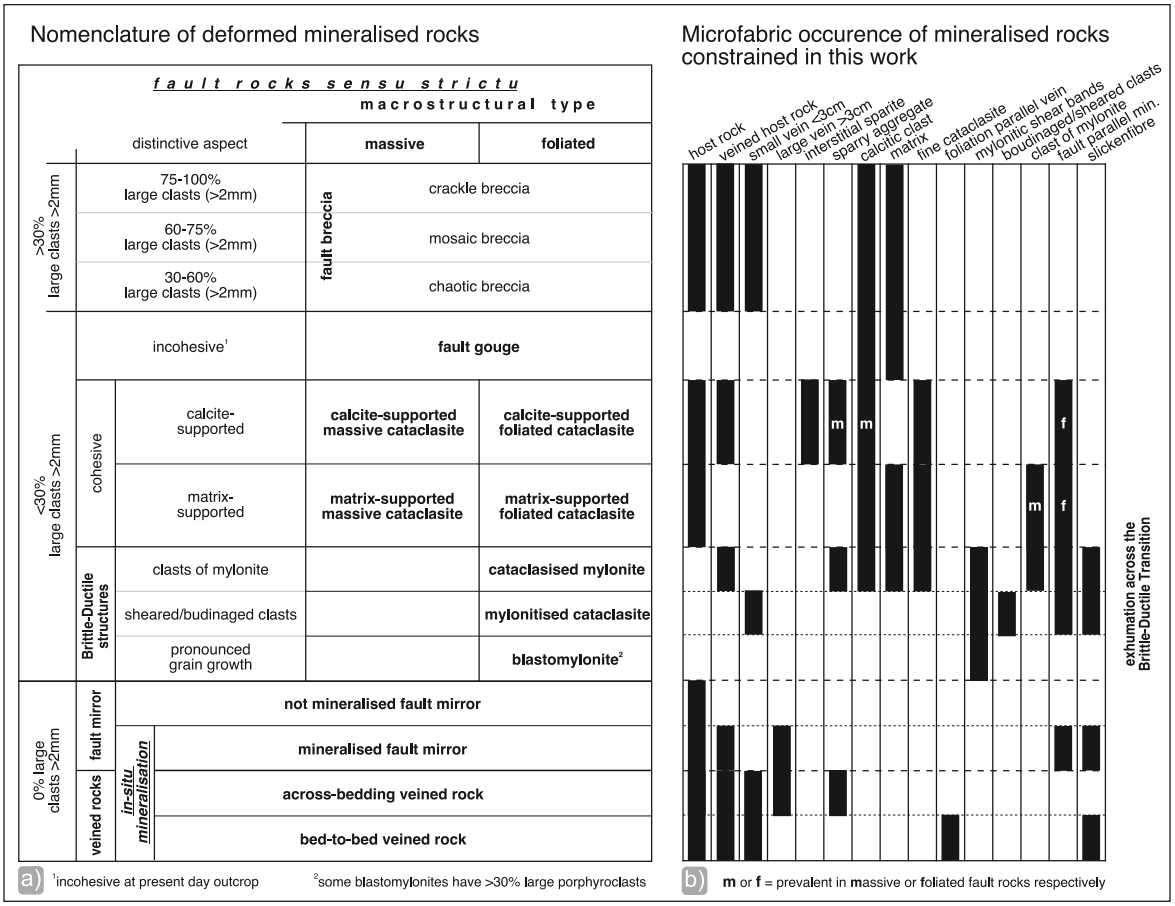

Fig. 2. a) Nomenclature of deformed mineralised rocks (modified after Woodcock and Mort, 2008). b) Microfabric occurrence of mineralised rocks as constrained in this study.

5) Matrix-supported massive cataclasite: coherent and massive fault rock, consisting of less than 30% of clasts greater than 2 mm, supported by matrix;
6) Matrix-supported foliated cataclasite: coherent, foliated fault rock with a pervasive internal organisation parallel to the main fault plane consisting of less than 30% clasts greater than 2 mm, mainly supported by matrix;
7) Blastomylonite: a highly recrystallized rock, rich in porphyroclasts (crystal size 10–50 μm);
8) Mylonitised cataclasite: a cataclasite whose clasts are sigmoids wrapped by micro shear bands made of recrystallized elongated crystals or presenting a pinch-and-swell shape that resembles a boudin;
9) Cataclasised mylonite: a mylonite whose remnant structure is preserved in isolated clasts, which are usually overprinted by multiple generations of veins and stylolites.

The *in situ* mineralised rocks consist of

10) Fault mirrors: smooth millimetre-thick surfaces hosting mineralisation that may be striated in the direction of relative motion between fault blocks;
11) Across-bedding veined rocks: rocks crossed by veins of calcite, generally at high dip angle, which cuts the bedding or the foliation;
12) Bed-to-bed veined rock: rocks crosscut by veins of calcite parallel or subparallel to bedding or main schistosity.

Finally, for each macrostructural fabric various microfabrics were recognized (Fig. 2b).

1) Host rock: portion of rock that tends to be undeformed, which in the case of veined host rock can be crossed by one or more veins and micro-veins (thickness <2 mm);
2) Veins: calcite mineralisations – euhedral and otherwise – of calcite within extensional or shear fractures, isolated or organised in groups, which crosscut the host rock. Depending on their width, the veins are also divided into large veins (>3 cm) or small veins (<3 cm);
3) Cement: calcite with a saccharoidal texture present in the interstices of fault rocks;
4) Sparry aggregates: coarse aggregates composed of millimetre to centimetre-sized subhedral crystals present within open or fault-sealed cavities;
5) Calcitic mineral clasts: often found in cataclasites;
6) Matrix: granular material <63 μm present between larger clasts;
7) Fine cataclasite: generic fault rock with 63 μm < d < 2 mm clasts that are indistinguishable from the matrix;
8) Mylonitic bands: white to grey bands of recrystallized calcite often containing porphyroclasts;
9) Sheared clasts: clasts with sigmoidal or boudinaged shape wrapped by shear bands;
10) Clasts of mylonites: isolated mylonitic elements (or of cataclasised mylonites) wrapped by matrix or cement;
11) Fault-parallel mineralisations: unstriated mineralisations parallel to fault surfaces;
12) Slickenfibres: fibrous and striated mineralisations on fault mirrors.

3.4. Carbonate carbon, oxygen, and clumped isotope geochemistry

The above classification was applied to all samples (see Table S2 in Supplementary Material) – in some cases representing multiple fabrics – taken from 97 localities, for a total of 263 microfabrics, which were classified and sampled to measure carbonate C and O stable isotopes. Details are given in the Supplementary Material.

3.5. Clumped isotopes modelling

A limitation of carbonate clumped isotope thermometry is the possible modification of the original temperature due to solid-state bond reordering when a sample that was formed at low temperatures is heated to temperatures >90–100 °C (e.g. Hemingway and Henkes, 2021). In this case, the measured $T\Delta_{47}$ reflects an apparent temperature ranging between the original temperature of formation and the maximum temperature experienced during burial (Henkes et al., 2014; Stolper and Eiler, 2015). On the other hand, samples formed at high temperatures (>200 °C) do not preserve the formation temperature but a lower "closure temperature" (Dennis and Schrag, 2010; Schmid and Bernasconi, 2010). For this reason, we have modelled the evolution of clumped isotope temperatures to evaluate possible alteration of the original compositions.

Solid-state bond reordering was modelled with the open-source python package "Isotopylog" (Hemingway, 2020, version 0.0.8). Reordering paths were calculated in the I-CDES reference frame using the transient defect/equilibrium model (Passey and Henkes, 2012; Hea14), the paired exchange-diffusion model (Stolper and Eiler, 2015; SE15) and the disordered kinetic model (Hemingway and Henkes, 2021; HH21). For the conversions between Δ_{47} and temperature, the calibration by Anderson et al. (2021) was used, validated within the temperature range from 0.5 to 1000 °C, and established using carbonate standardisation (Bernasconi et al., 2021). Depending on the length of the modelled time interval and the complexity of the t-T path, models were calculated with 1000–20000 timesteps (nt). As uncertainty on the initial Δ_{47} composition, we took the 95% confidence interval on the measured Δ_{47} composition of each sample individually. The SE 15 model, which is the only model where reordering depends on the isotopic composition of the material, used the average sample values of 0.5 and −11‰ for $\delta^{13}C$ and $\delta^{18}O$ respectively. Other parameters were left at the default values (iso_params = 'Brand', nnu = 400, z = 6).

The modelling software takes the formation temperature (as initial Δ_{47} composition) and the modelled burial-exhumation trajectory of a samples as input and outputs a prediction for the clumped isotope temperature this sample would show today, after potentially experiencing reordering (T_{mr}). Thus, to arrive at a modelled formation temperature (T_{mf}) from the calculated clumped isotope temperature ($T\Delta_{47}$) requires iteratively matching the T_{mr} to the $T\Delta_{47}$. As estimation of the uncertainty on the T_{mf}, we give the ranges of formation temperature inputs that result in predicted clumped final temperatures that fall in the 95% confidence intervals of the $T\Delta_{47}$ when modelled with the disordered kinetic model.

4. Results

4.1. Apatite fission track data

Four new apatite fission track (AFT) ages were obtained (Fig. 1; Table 2) ranging from 4.2 ± 0.8 Ma (2σ) near the Pennine Basal Thrust (PBT; MR P 494) to 9.2 ± 1.7 Ma for sample 85LC from the Ultrahelvetic nappes in the Rawil Depression. The mean track lengths vary from 13.8 to 14.6 μm and mean Dpar values from 3.3 to 3.7 μm, indicating moderate to fast cooling and enhanced Cl contents for the dated apatite grains. Notably, the AFT age for sample 85LC (9.2 ± 1.7 Ma) significantly exceeds a previous age of 5.6 ± 1.4 Ma by Soom (1990) from the same location. All ages are cooling ages, as the maximum Alpine metamorphic temperatures (Girault et al., 2020) are consistently above the apatite partial annealing zone.

4.2. Zircon (U–Th)/He data

Results of the ZHe analysis on four Fish Canyon Tuff (FCT) age-standard grains and our samples are given in Table 3 and Fig. 1c and d. The FCT age standard grains give ages ranging between 28.0 and 31.5 Ma, with a mean age of 29.3 Ma and 2σ of 2.2 Ma (corresponding to an 8% uncertainty). We analysed one to three zircons from ten samples, for a total of twenty-two single grains. The single grain ZHe ages show a wide range, from 10 Ma to 215 Ma. This range extends to ages much older than the depositional age of the dated samples, indicating that for some samples the temperature and duration during depositional or tectonic burial were not sufficient to fully reset the detrital ages. A rough criterion to discriminate between ages that were potentially reset, partially, or non-reset can be based on a comparison between the cooling and the depositional age of the dated sample: a cooling age much younger than the depositional age likely indicates total age resetting, while a cooling age overlapping with or older than the depositional age suggests partially to non-resetting. For instance, sample 83LC is from a Middle Jurassic sandstone of the Wildhorn Nappe, the stratigraphically oldest and currently southernmost unit of our study, and has a ZHe age younger than the depositional age. However, single grain ages span a wide range between 10 Ma and 73 Ma, indicating partial age reset. Sample 138LC and 90LC are from Lower Cretaceous sandstones of the Wildhorn Nappe but show a large age scatter from Jurassic to Eocene, with four grain ages ≥78 Ma. Only one grain age of 46.5 ± 0.3 Ma

Table 2
New apatite fission track data of the Rawil Depression.

Sample ID and Locality	Mineral and No. Crystals	Spontaneous ρs (Ns)	Induced ρi (Ni)	$P\chi^2$	Dosimeter ρd* (Nd)	Central FT Age (Ma) (-2σ/+2σ)	Mean Track Length	S.d. of distribution (No. Tracks)	Mean Dpar (Dpar range)
85LC Plaine Morte	apatite (22)	0.018 (132)	0.450 (3399)	90%	13.78 (4238)	9.2 (−1.5/+1.8)	13.97	1.07 (17)	3.43 (2.65–4.87)
MR P 488 Lämmerenboden	apatite (34)	0.013 (170)	0.434 (5924)	63%	13.45 (13,561)	6.6 (−1.0/+1.1)	14.61	1.12 (77)	3.30 (2.10–4.87)
MR P 490 Tsanfleuron	apatite (40)	0.019 (275)	0.614 (8771)	99%	13.48 (13,588)	7.3 (−0.9/+1.0)	13.81	1.48 (61)	3.48 (2.74–5.24)
MR P 494 La Muraz	apatite (40)	0.009 (112)	0.486 (6229)	100%	13.55 (13,662)	4.2 (−0.7/+0.9)	13.80	1.62 (31)	3.18 (1.84–4.27)

Notes.
(i) Track densities are ($x10^7$tr cm^{-2}), * = ($x10^5$ tr cm^{-2}) numbers of tracks counted (N) shown in brackets.
(ii) analyses by external detector method using 0.5 for the 4π/2π geometry correction factor.
(iii) ages calculated using dosimeter glass CN-5 for apatite with $\zeta_{CN5} = 344 \pm 5$.
(iv) $P(\chi^2)$ is probability for obtaining χ^2 value for v degrees of freedom, where v = no. Crystals - 1.
(v) track length and Dpar data are given in 10^{-6} m, S.d. = 1σ standard deviation.

Table 3
New zircon (U–Th)/He data of the Rawil Depression.

Sample ID	Mass	He	^{238}U	^{232}Th	eU	Raw age	L	W1	W2	H	Fzac	Corrected age	Age error	Error
	µg	fmol	fmol	fmol	ppm	Ma	µm	µm	µm	µm		Ma	Ma	%
LCfctz1	2.55	115.40	3951.03	2049.71	416.01	20.18	148.26	70.16	76.59	34.78	0.72	28.05	0.24	1.19
LCfctz2	3.39	216.02	6452.89	3352.83	510.01	23.12	187.17	79.59	69.00	40.76	0.73	31.51	0.23	0.98
LCfctqz3	5.53	395.86	11891.46	6850.71	582.77	22.73	224.09	83.50	90.59	50.07	0.77	29.48	0.30	1.33
LCfctz4	4.00	219.41	7127.49	3601.78	476.17	21.32	180.46	91.53	76.54	43.22	0.75	28.29	0.29	1.34
60LCz1	2.21	55.50	3295.34	808.45	376.98	12.34	148.96	70.25	62.74	30.74	0.70	17.54	0.09	0.71
60LCz2	2.64	87.43	3123.76	1244.39	309.42	19.83	153.79	84.90	63.03	35.77	0.72	27.55	0.14	0.71
93LCz2	3.39	191.50	6688.81	788.20	485.15	21.55	151.58	91.40	82.07	40.70	0.75	28.70	0.33	1.53
93LCz3	2.99	16.52	1083.49	107.44	88.85	11.54	164.08	79.78	70.35	37.14	0.73	15.75	0.09	0.75
93LCz4	1.57	51.89	2081.16	684.22	341.02	17.93	127.68	61.36	65.30	32.45	0.68	26.45	0.18	1.03
99LCz1	3.20	230.41	11846.47	1313.95	909.75	14.67	167.34	80.90	77.95	43.64	0.74	19.79	0.16	1.08
99LCz2	5.09	273.18	8284.46	2844.54	420.49	23.62	201.92	88.97	89.58	48.38	0.77	30.61	0.22	0.93
128LCaz2	3.39	47.86	2633.13	818.63	199.13	13.13	164.69	87.90	71.84	36.82	0.74	17.68	0.13	1.02
85LCz1	3.35	62.04	3436.62	1794.89	274.91	12.47	195.96	80.80	64.62	43.39	0.73	17.11	0.11	0.86
138LCz1	3.34	515.16	2999.98	920.23	230.54	122.89	176.03	78.78	66.47	29.22	0.73	167.97	1.29	1.05
138LCz2	3.52	820.98	3760.59	991.11	271.76	157.19	216.03	68.66	72.74	48.45	0.73	215.41	1.57	1.00
138LCz3	2.23	265.29	5778.30	2120.67	674.05	32.70	147.45	62.67	70.78	29.61	0.70	46.52	0.32	0.97
57LCz1	2.92	602.36	9469.11	2077.78	817.09	46.71	177.92	73.81	67.80	39.42	0.72	64.53	0.44	0.95
57LCz2	2.73	159.23	1389.70	427.33	130.67	82.28	218.92	63.86	58.58	46.56	0.70	118.06	0.78	0.95
79LCz1	1.72	121.21	3321.34	739.28	486.36	26.83	124.46	68.22	60.29	25.89	0.69	39.14	0.26	0.98
79LCz2	3.02	308.63	3722.06	1013.50	313.32	60.12	200.72	68.86	69.25	48.24	0.72	83.45	0.81	1.34
90LCz1	3.14	717.14	6404.30	1322.88	512.13	82.19	145.76	78.50	85.52	33.90	0.74	110.72	1.14	1.39
90LCz2	4.69	263.43	2838.80	2387.61	172.95	59.93	157.40	102.55	89.64	35.79	0.77	77.82	0.70	1.16
83LCz1	1.69	8.28	875.82	302.59	134.25	6.78	137.36	64.99	61.07	34.46	0.68	9.96	0.05	0.81
83LCz2	4.32	122.44	1403.93	1513.45	97.11	53.90	207.90	75.74	75.74	34.57	0.74	72.46	0.38	0.71

(138LCz3) indicates minor partial age resetting. Samples 57LC and 79LC are from Eocene sandstones of the Wildhorn Nappe: three grains give ZHe ages older than the depositional age and one grain an Eocene age (39.1 ± 0.3 Ma), suggesting partial resetting. Samples 93LC, 60LC and 99LC are from Cretaceous and Eocene sandstones of the Diablerets Nappe in the Sanetsch area (Fig. 1). All ZHe ages are younger than their depositional ages and scatter over a relatively narrow age range from 16 Ma to 31 Ma. Samples 128aLC and 85LC are from upper Eocene – lower Oligocene sandstones of the lowermost Doldenhorn Nappe and uppermost Ultrahelvetic nappes, respectively. Only one grain could be dated for each sample (17.1 ± 0.1 Ma and 17.7 ± 0.1 Ma, respectively) and they are both markedly younger than the depositional age of their stratigraphic units.

A significant portion of the dated zircons show a positive correlation between grain size and ages (Table 2 and Fig. 3a and b). Sample 93LC shows a positive correlation between age and eU (= effective U, proportional to the radiation damage induced by the concentration of both U and Th, Shuster et al., 2006) (Fig. 3c and d). While these correlations are not systematic, as we dated more than two grains in two samples only, they are consistent with the fact that He diffusion is controlled not only by the cooling history but also by grain size and eU. Thus, the large scatter of the ZHe ages from the Wildhorn Nappe could be interpreted as reflecting a variable degree of resetting, mostly due to differences in grain size (Fig. 3a and b) and radiation damage (Fig. 3c and d). In the samples from the Diablerets Nappe, which are fully reset, the age scatter may possibly relate to a slow cooling rate in the PRZ, which makes the He diffusion more sensitive to the effect of grain size and radiation damage.

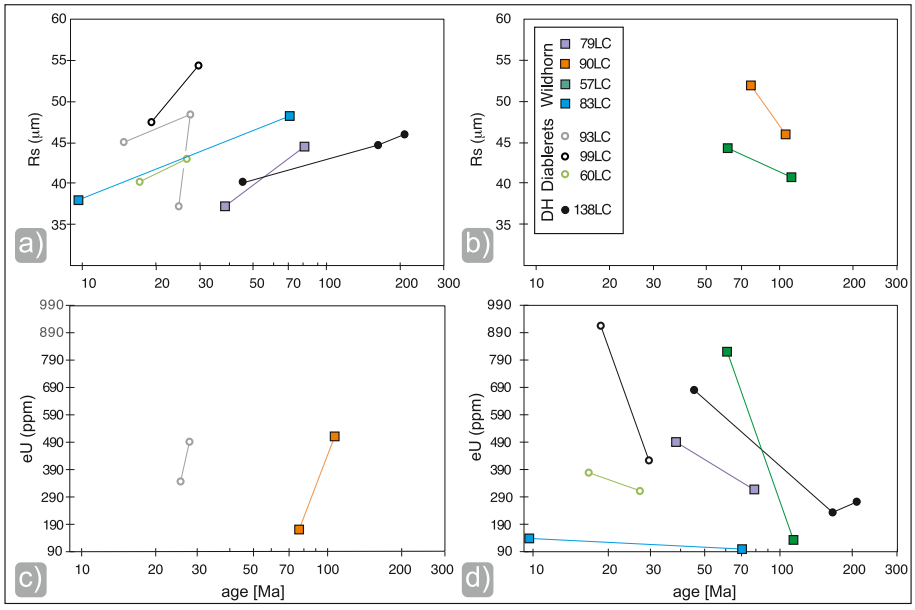

Fig. 3. Positive correlation between grain size and ages from different nappes. DH = Doldenhorn Nappe. a-b) Rs vs time. c-d) eU vs time.

4.3. Thermal modelling

Modelling-derived time-temperature envelopes are shown in Fig. 4. They show fast burial and heating subsequent to sedimentation and peak metamorphic conditions reached after 26 Ma (cf. section 5.2), depending on the nappe. ZHe ages of around 16 Ma suggest that cooling started during late nappe-stacking (Kirschner et al., 2003). Closure of the ZHe system around the same time across the Rawil Depression axis suggests contemporaneous closure in the axial region, but distinctly later ZHe closure in the backlimb region (cf. Fig. 1d). AFT ages are significantly younger than ZHe ages, suggesting a thermal plateau or period of slow cooling during or after ZHe closure (see section 5.1). Modelled results for late cooling rates (Fig. 4a) differ slightly from nappe to nappe. In the axial region they increased in a time window from 10 to 6 Ma (contemporaneously with closure of the ZHe system in the backlimb region). For the Sanetsch area (Fig. 4b), cooling rates might have slowed down from 5 to 3 Ma, but then accelerated during the Quaternary, as shown by Valla et al. (2012). Also, slow cooling rates are suggested during the last 5 Myr for the Gemmi region (Fig. 4c). Similar trends have already been reported from the Morcles Nappe (Kirschner et al., 1996) and from Brigerbad (Valla et al., 2016) (Fig. 1a). Since the results for part of the youngest thermal evolution are located below the sensitivity of the apatite partial annealing zone (PAZ), they must be taken with caution. For the sample from the backlimb region (Fig. 4d), ZHe and AFT ages are distinctly younger. The thermal modelling also used thermochronologic data from the Pennine Basal Thrust (Cardello et al., 2019). Considering the time range from closure of the ZHe system (10 Ma; Sample 83LC) to the present, modelling included AFT ages from the by then coupled Sion-Courmayeur Zone (Sample MR P 494). Cooling rates increase prior to 6 Ma and possibly during the Quaternary, when glacial erosion excavates the major valleys (Valla et al., 2011). However, the modelling envelope would also support constant cooling during the last 6 Myr.

Regarding the Wildhorn Nappe, we deduced its exhumation path by

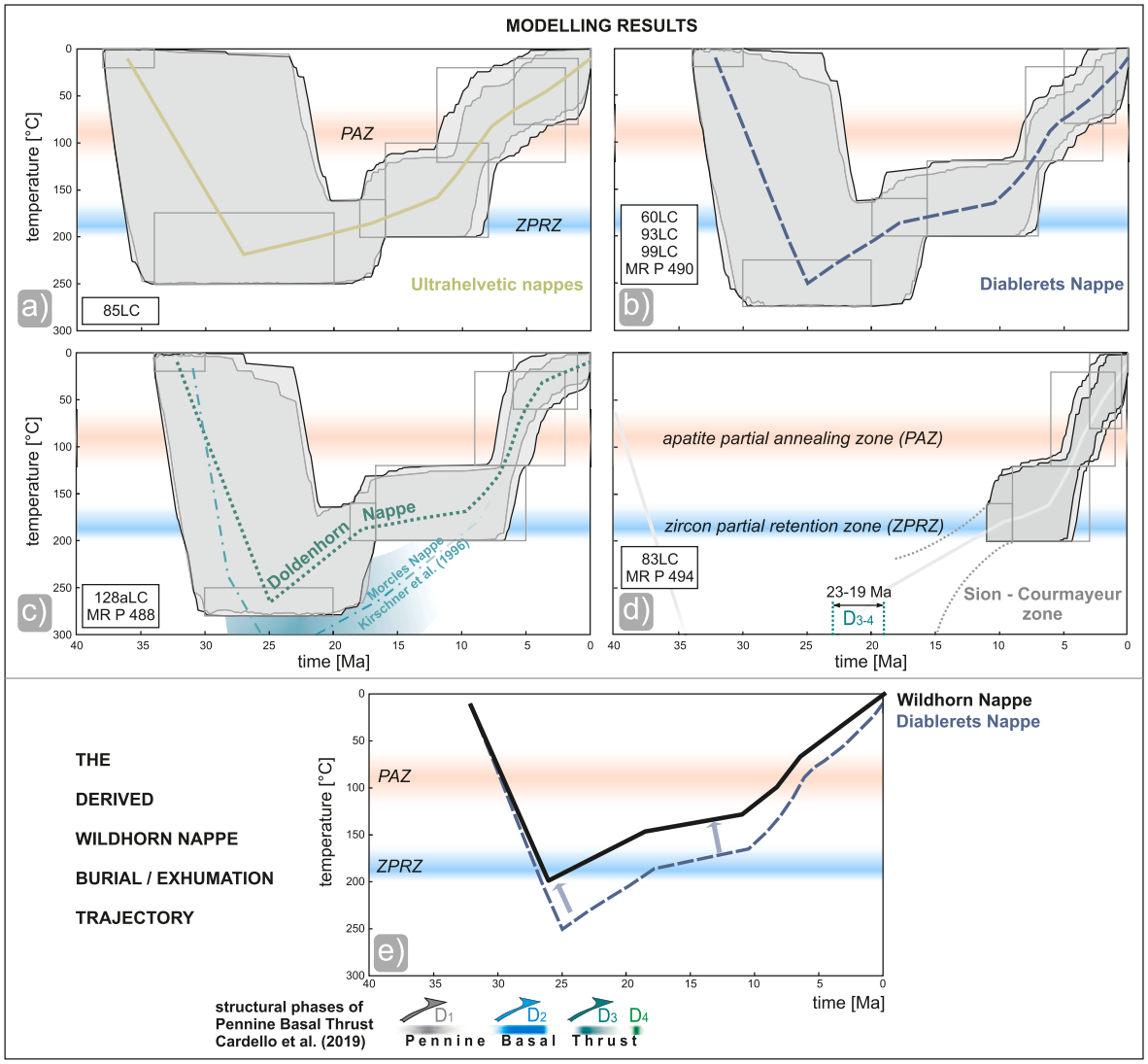

Fig. 4. Thermal modelling results from different nappes constrained by the youngest syn-orogenic deposits preceding burial, by peak metamorphic temperatures (cf. section 2 and 3); and the available low-T thermochronologic data for cooling during exhumation. Grey areas show the envelope of good paths (goodness of fit >0.5), while areas of light grey colour underneath correspond to the envelope around acceptable paths (goodness of fit >0.05) (Ketcham, 2005). Thicker lines correspond to the weighted mean path of all good paths. Early cooling constraints are based on ZHe ages (this study, based on a zircon partial retention zone after Reiners et al., 2005). Thermal constraints based on AFT data are restricted to the last three time-temperature boxes crossing or covering part of the apatite partial annealing zone (reddish zone between 120 and 60 °C). Blue time-temperature zone in c) is the thermal history proposed by Kirschner et al. (1996) for the Morcles Nappe. e) Burial/exhumation trajectory of the Wildhorn Nappe derived from the Diablerets Nappe, as explained in section 4.3. (For interpretation of the references to colour in this figure legend, the reader is referred to the Web version of this article.)

graphically flattening the Diablerets Nappe curve, as indicated by the blueish arrows in Fig. 4e. In this process, the lower peak temperature was adjusted to 200 °C, in agreement with a partial resetting of the ZHe system within the Wildhorn Nappe. Finally, the peak temperature was repositioned to coincide with the end of most of the PBT activity (see section 2), under the assumption that this event corresponds to the burial peak associated with D_2 around 26 Ma (Cardello et al., 2019).

4.4. Microstructures and isotopic data

The spatial distribution of analysed samples for stable isotopes is shown in Fig. 5a. These samples have been categorised into four groups based on their carbon and oxygen isotopes. In the $\delta^{13}C$ – $\delta^{18}O$ plot, we observe a main cluster with $\delta^{13}C$ ranging between 0 and 2.5‰, and $\delta^{18}O$ between −2 and −8‰ (Fig. 5b). This cluster corresponds to typical Mesozoic marine carbonates and is mainly determined by samples from the Wildhorn Nappe.

Fig. 5c shows the same dataset but sorted into macrostructural groups, such as shear zones, different faults types and veined rocks. Notably, the isotope data demonstrate two distinct trends. The first trend exhibits the most negative values for the samples along the PBT ($\delta^{13}C$ = −8‰, $\delta^{18}O$ = −13‰). In particular, structures in the south-eastern part of the Wildhorn Nappe tend to show negative values for $\delta^{18}O$ (−13‰). While the first trend (indicated by the orange arrow in Fig. 5c) is represented by thrusts and veined rocks, the main cluster encompasses all macrofabrics including ductile shear zones. The second

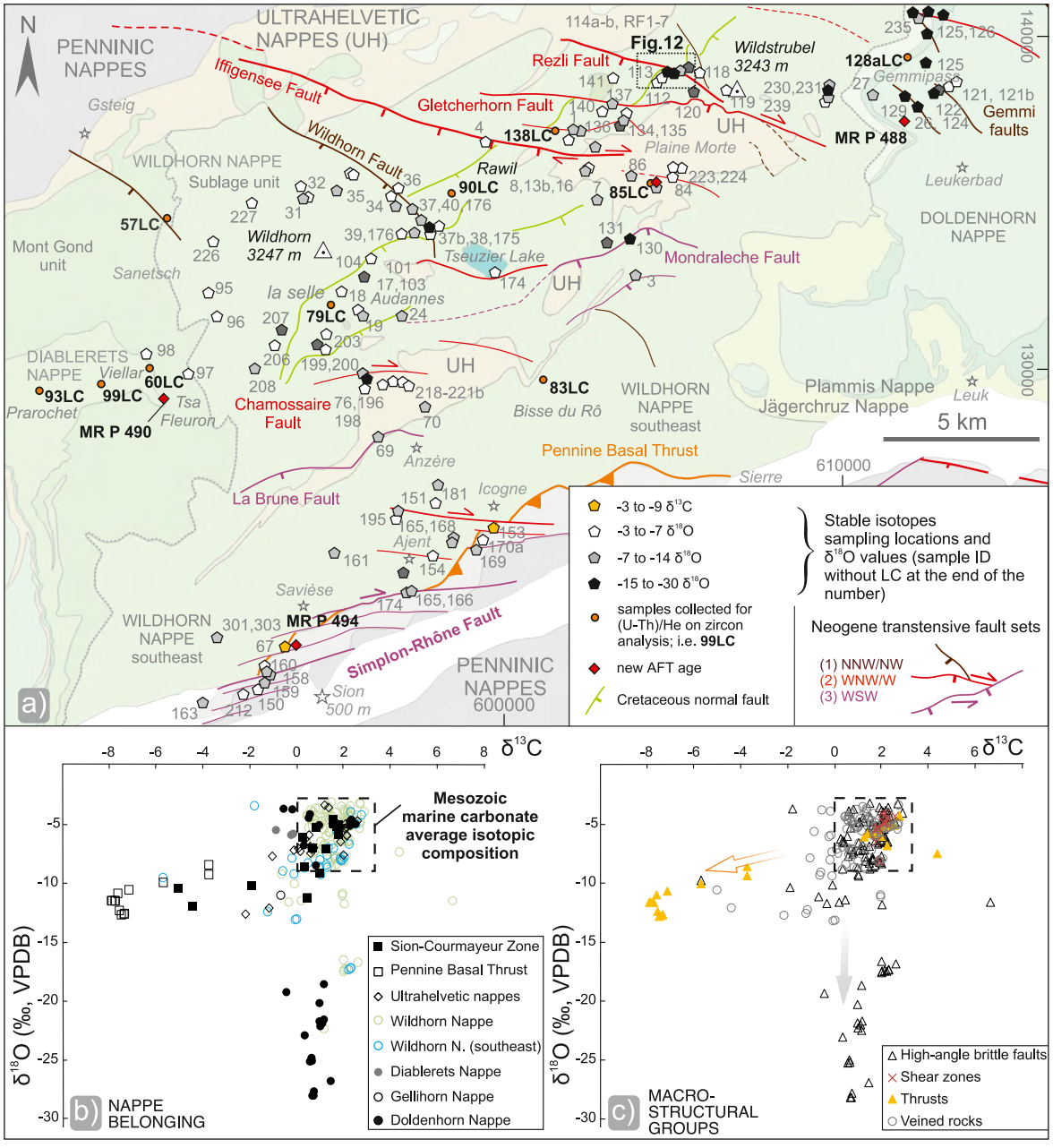

Fig. 5. a) Tectonic map showing the sampling locations for ZHe, stable isotopes and clumped isotopes in Swiss coordinates (location of map outlined in Fig. 1a). Neogene transtensive faults from Cardello and Mancktelow (2015). Stable isotopes are divided into four categories representative of the degree of rock buffering in the measured carbonate. In the north of the map, a dotted box highlights the sampling area near the Rezli Fault (Fig. 12), data from which are described in section 4.5. b) Isotopic trends across different nappes. c) Graphs of stable isotopes keyed by macro-structural type. Marine carbonates are prominently clustered in the dashed black box.

trend (grey arrow in Fig. 5c) reaches as far as $\delta^{18}O = -28‰$ and is mostly found in faults that cut across the Doldenhorn Nappe near the Gemmi Pass (Fig. 5a).

An example of a variety of host rocks crossed by different type of extensional to shear veins provides insights into the mineralised textures in Fig. 6a-l, together with their outcrop mesostructures (Fig. 6a–d, g, j), fabric from polished thin-section blocks (Fig. 8b–e, h, k) and polarized light thin-section photomicrographs (Fig. 6c–f, i-l). Bed-to-bed veins show different types of calcite twinning and widespread recrystallization and interfingering grain boundaries of different grain sizes (Fig. 6c). This is more extreme in foliation-parallel veins reworked by pressure solution (Sample 301LC) than in veins preserving a higher angle with

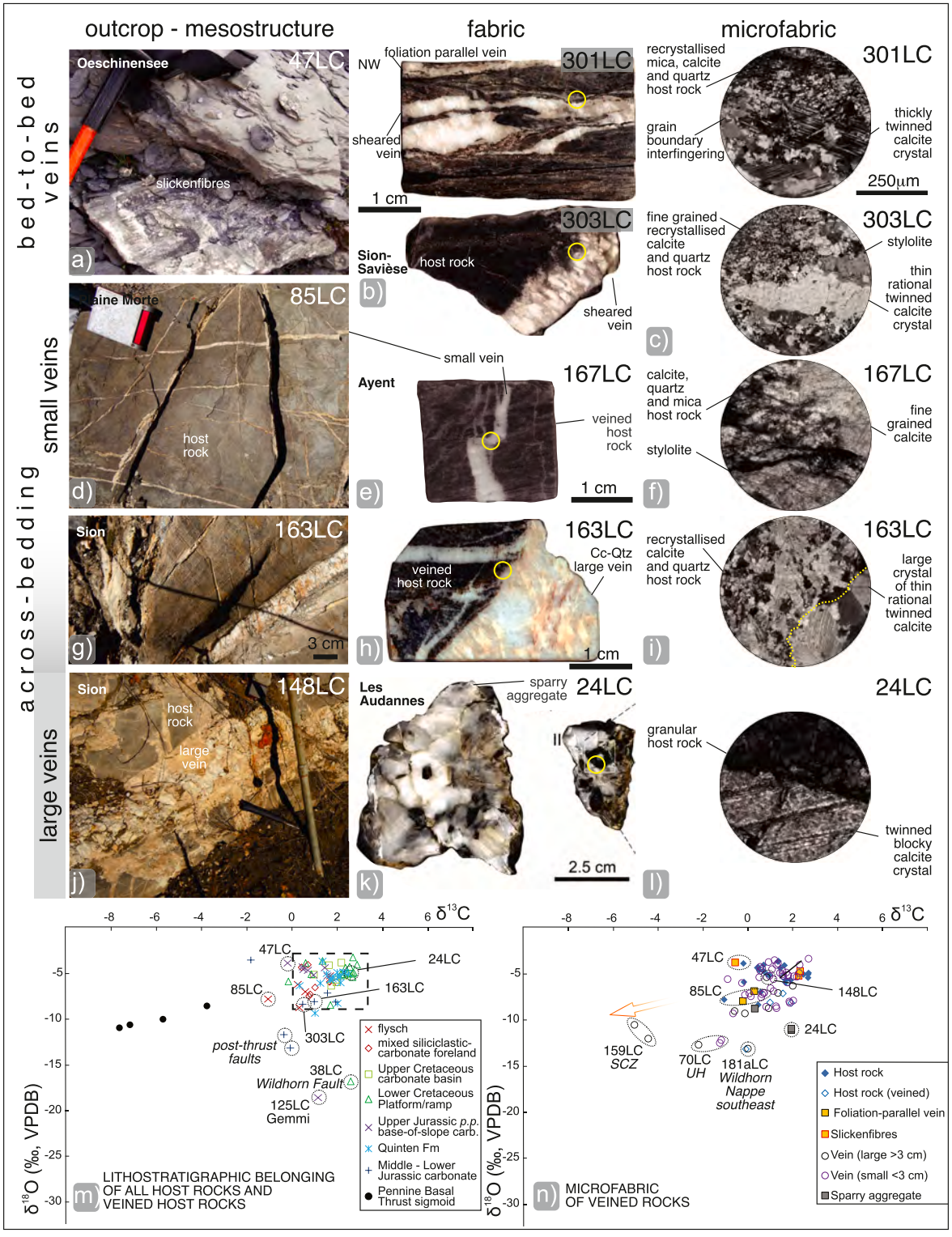

Fig. 6. a-l) Field, hand sample and microstructural texture examples showing the different microstructures of bed-to-bed and across-bedding veins, as classified in Fig. 2. The hand samples, including polished thin-section blocks, show the internal fabric indicative of the sampled areas (yellow circles), which were further explored under an optical microscope. Corresponding descriptions of microstructures are provided in c, f, i-l. Several types of grain boundaries and twins are recognized. Note that the scale is consistent for all observed microstructures. m-n) $\delta^{18}O$ vs $\delta^{13}C$ VPDB diagrams display m) host rocks from various groups of formations and n) from different microstructures also categorised in Fig. 2. SCZ: Sion-Courmayeur Zone. UH: Ultrahelvetic nappes.

the foliation (Sample 303LC). All thin-section examples are from recrystallized vein structures and veined host rocks but sample 24LC (Wildhorn Nappe), which shows a granular texture, preserved clasts that are separated by intervening blocky calcite (Fig. 6l). Isotopic signatures of host-rock and veined host-rock belonging to different lithostratigraphic groups are shown in Fig. 6m, together with the specific isotopic plot of the veined rocks microfabric (Fig. 6n). Note that only a few, usually large, veins from nappes in the backlimb region and host rocks from post-thrust faults plot outside the main cluster.

Examples from thrust faults are shown in Fig. 7 a-i. The PBT fabric shows sigmoidal lithons with a recrystallized and veined host rock, which itself is affected by foliation-parallel calcite-quartz veins with hematite, limonite, and pyrite. Ghosts of folded calcite bands are locally preserved within a very fine-grained orange calcite (Fig. 7c), while high-angle veins of quartz and calcite occur interfingering with the veined host rock. The rock fabric of Helvetic thrust rocks is a foliated tectonite (Fig. 7h) hosting deformed and recrystallized clasts with a pinch-and-swell morphology enveloped by calcite of finer grain size (Fig. 7i),

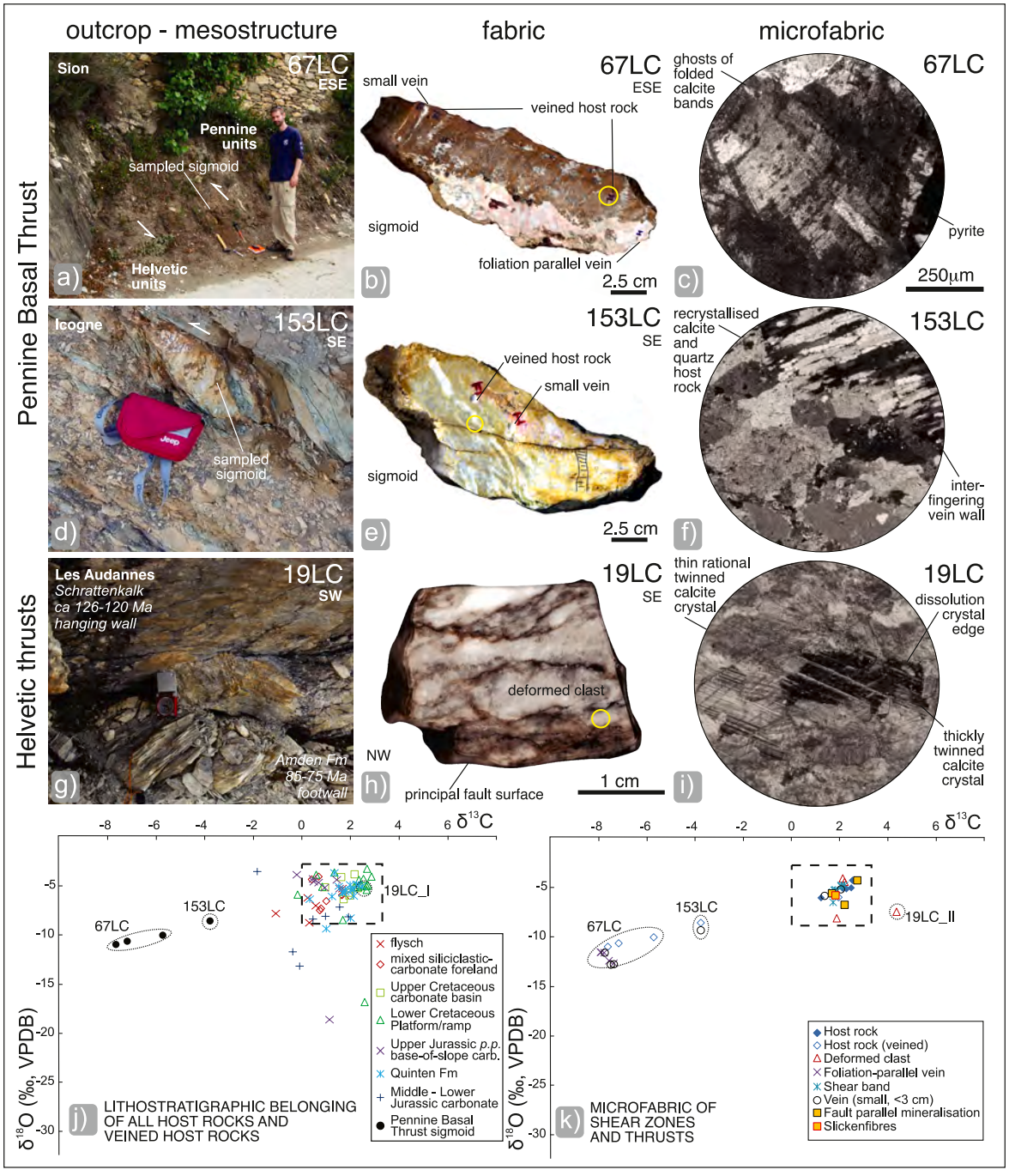

Fig. 7. a-i) Field, hand sample and microstructural texture examples to illustrate the different microstructures of thrusts. In particular, the Pennine Basal Thrust (PBT) exhibits entirely recrystallized sigmoids intersected by millimetric to centimetre-wide shear veins (a–f), whereas Helvetic thrusts display BDT typical structures with sheared clasts and pressure solution seams (g–h). The sampled areas of these specimens are marked, and their microstructures investigated in the adjacent areas (yellow circles). Note that the scale is consistent for all observed microstructures, and that the internal structure is the result of overprinting recrystallization (e.g., c, d, i). j-k) $\delta^{18}O$ vs $\delta^{13}C$ VPDB diagrams depicts j) host rocks from various groups of formations and k) from various microstructures categorised in Fig. 2. The isotopic composition of the samples presented above is also highlighted. (For interpretation of the references to colour in this figure legend, the reader is referred to the Web version of this article.)

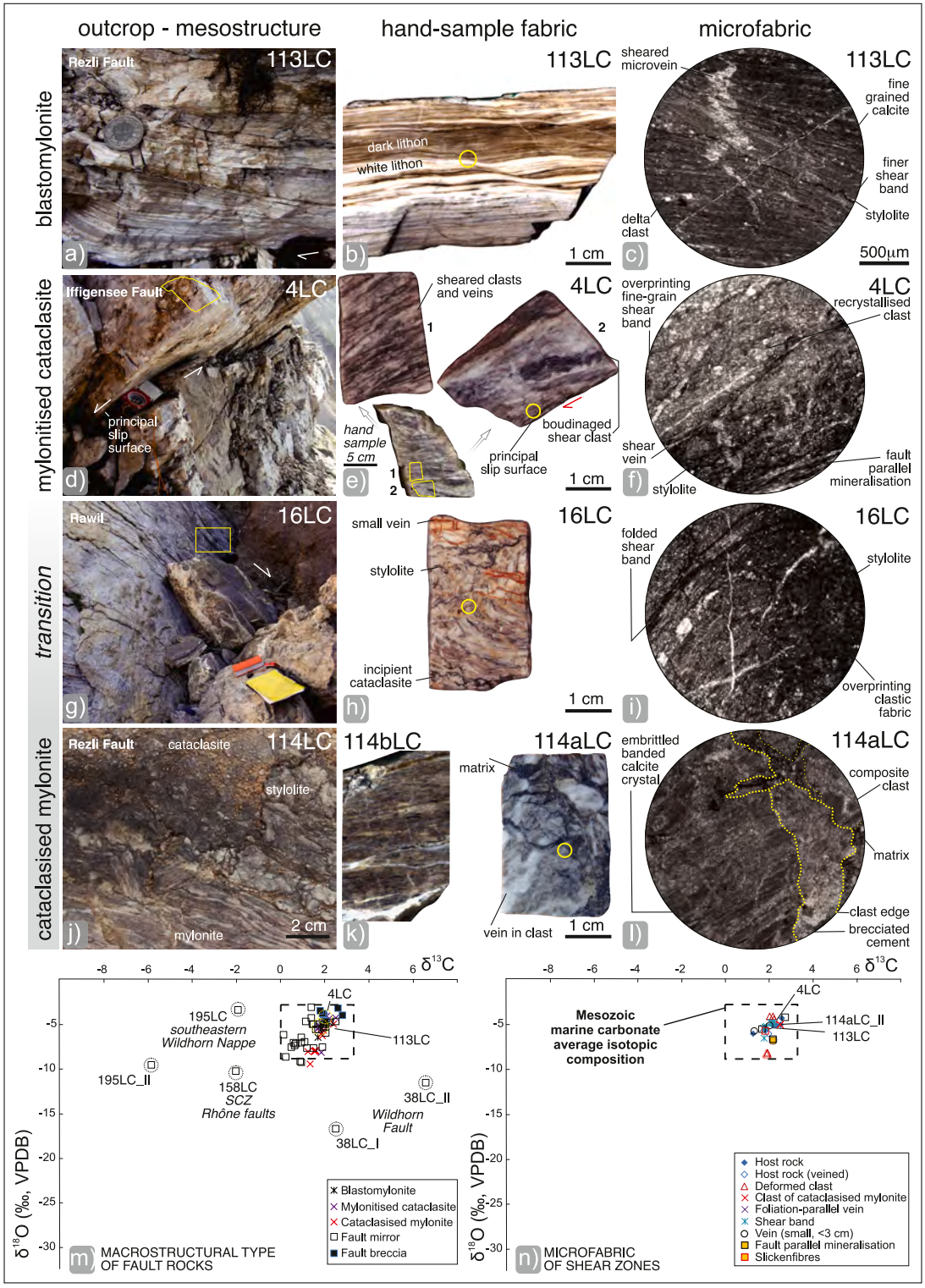

Fig. 8. a-i) Field, hand samples and microstructural texture examples showing the distinct microstructures associated with the BDT. The hand samples and polished thin-section blocks were further examined under an optical microscope. Note that the scale is consistent for all observed microstructures, and yellow boxes on field images and on the hand sample indicate the locations of microstructures categorised in Fig. 2. Sample 113LC is dominated by dynamically recrystallized calcite in shear bands (a–c), while the two 4LC thin-section blocks, taken from the one hand sample presented, show internal heterogeneity with clasts that are dynamically recrystallized (d–f). Sample 16LC and 114aLC respectively display an internally folded and cataclasised structure that, at the microscale, is slightly to more severely overprinted by a cataclastic fabric (g–i). Notably, the inherited blastomylonitic structure, although embrittled, can still be found in clasts (j–l). m-n) $\delta^{18}O$ vs $\delta^{13}C$ VPDB diagrams display m) diverse hand-sample structures and n) microstructures of shear zones within the main cluster (dashed black box). (For interpretation of the references to colour in this figure legend, the reader is referred to the Web version of this article.)

locally preserving aggregates of thin rational or single thickly twinned calcite crystals. As shown in Fig. 7j and k, the isotopic composition of the vein mineralisation generally corresponds to that of the host rocks, except for the PBT samples (67LC and 153LC) and the recrystallized and deformed clast of sample 19LC_II (see section 5.2).

Brittle-ductile rocks encompass transitional classes, represented by blastomylonites and microstructural types transitioning to cataclasites. The best-preserved example of the ductile end-member is depicted in Fig. 8a–c, showing well-pronounced crystal growth very marginally overprinted by intervening microveining and pressure solution (Fig. 8c). The mylonitised cataclasites (Fig. 8d–f) are characterised by finely recrystallized cataclasites, where clasts are typically stretched or boudinaged and recrystallized together with their matrix (Fig. 8f). The cataclasised mylonites (Fig. 2) can be distinguished by the occurrence of angular clasts of mylonites folded and overprinted by veins and stylolites, with unrecrystallised matrix preserved within the major clasts (Fig. 8g–i). The cataclasised mylonites can constitute angular clasts (Fig. 8j-l), which may preserve, although embrittled, shear-banded crystals of calcite. Further microstructural BDT examples are shown in section 4.5. Examining the related C and O stable isotope plots (Fig. 8m-

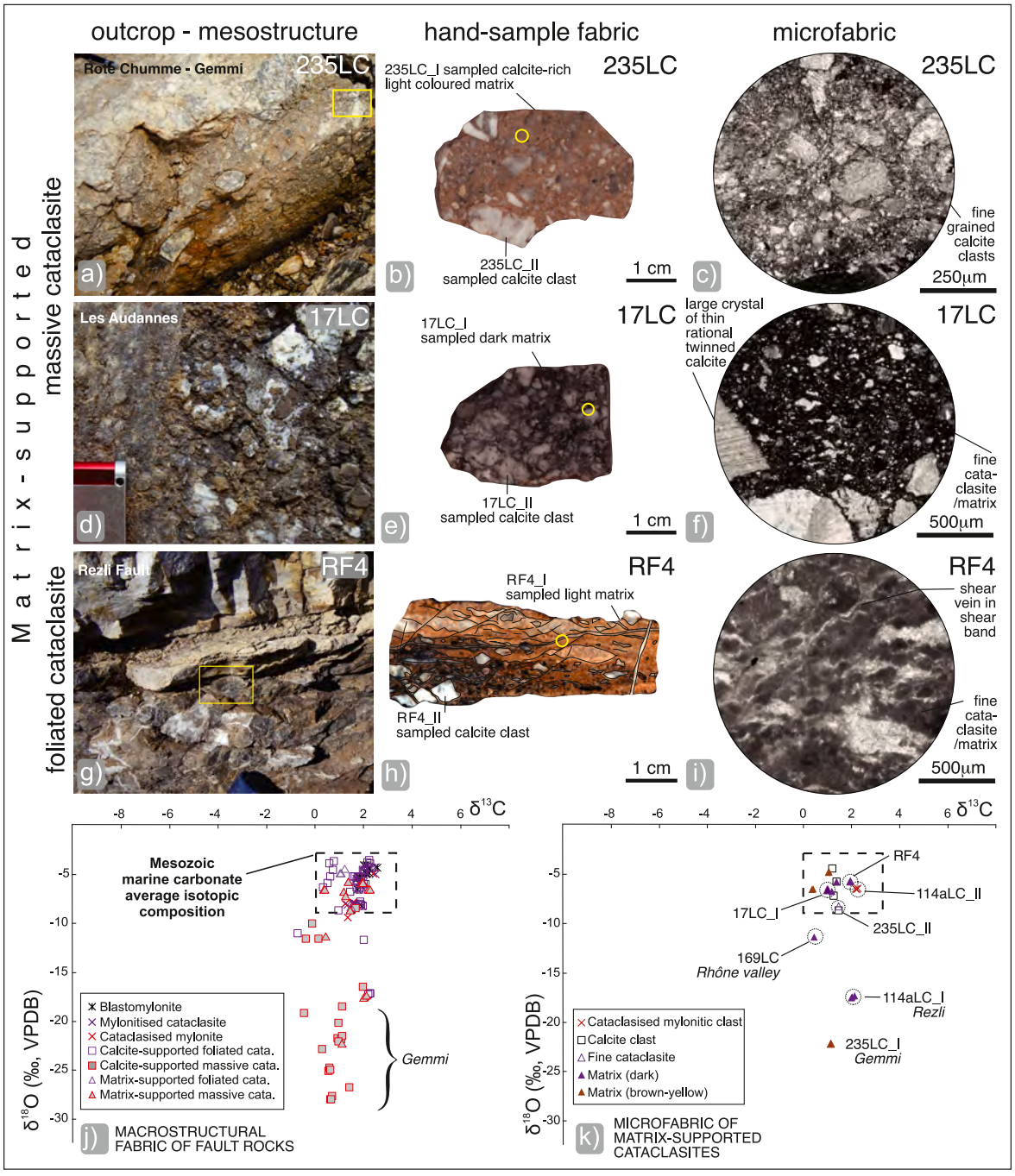

Fig. 9. a-f) Field, hand samples and microstructural texture examples showing the distinct microstructures associated with matrix-supported cataclasites. Polished thin-section blocks show the internal massive (a–f) or foliated fabric of the sampled areas (g–i), which were further explored under an optical microscope (yellow circles). In both end-members, the matrix has very mixed and fine-grained components (c, rich in calcite clasts; d, having more clay), which is affected by shear veins and asymmetric boudinage in the foliated case (i), while clasts are little overprinted by recrystallization. j-k) $\delta^{18}O$ vs $\delta^{13}C$ VPDB diagrams display j) diverse hand sample structures of high-angle faults and k) microfabric categorised as in Fig. 2. Notably all foliated faults plot within the main cluster (dashed black box), while only three specimens from matrix-supported massive-cataclasites faults plot outside of the main cluster. (For interpretation of the references to colour in this figure legend, the reader is referred to the Web version of this article.)

n) reveals that brittle-ductile rocks are clustered together within the main cluster, as they are isotopically indistinguishable from the host rock, while some fault mirrors plot separately outside of it.

In matrix-supported cataclasites, the matrix appears generally brownish-yellowish or dark, exhibiting an internal massive or planar fabric that is richer in very fine-grained calcite clasts (Fig. 9a–c) or dark clay (Fig. 9e and f). The microstructure of matrix-supported foliated cataclasites indicates that recrystallization is rather confined to the intervening sheared veins (Fig. 9g–i). As shown in Fig. 9j, most matrix-supported cataclasites plot within the main cluster, while in Fig. 9k, some matrix material has an isotopic composition transitional between the main cluster and lower $\delta^{18}O$ values (i.e., samples 169LC and 114aLC_I). Conversely, others like RF4 or 17LC plot within the main cluster, together with mylonitic clasts such as 114aLC_II.

The calcite-supported massive cataclastic example (Fig. 10a–c) is cemented by a sparry aggregate or is composed of a very fine-grained matrix comprised of submillimetric calcite clasts (Fig. 2). The foliated variant (Fig. 10d–f) contains clasts that remain clearly recognizable,

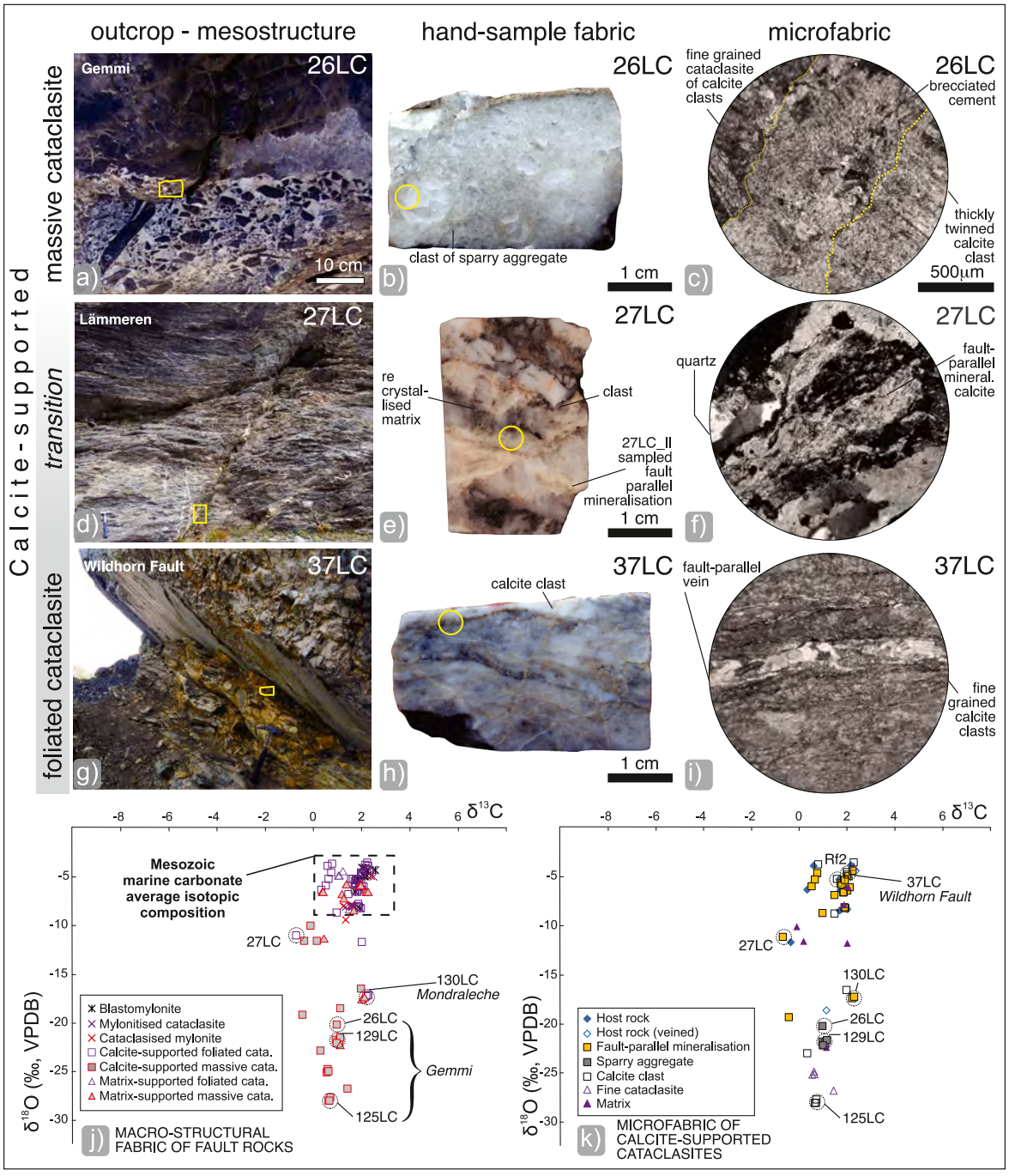

Fig. 10. a-i) Field, hand sample and microstructural texture examples exhibiting distinct microstructures associated with calcite-supported cataclasites. The polished thin-section blocks show the sampling areas, which were further explored under an optical microscope (yellow circles). Notably, massive cataclasite shows typical hydrofracturing with re-brecciated cements (a–c), while foliated cataclasites show recrystallized cements at fault-parallel mineralisations (d–f), the most extreme cases developing at the expense of still visible fine-grained calcite clasts that were spared from complete recrystallization (g–i). j-k) $\delta^{18}O$ vs $\delta^{13}C$ VPDB diagrams display g) different hand sample structures within faults from the Gemmi region (Fig. 5a) plotting far from the main cluster (black dashed box), and h) micro-structures sampled and categorised as in Fig. 2 show that fine cataclasite, calcite clasts and sparry aggregates reach low-VPDB $\delta^{18}O$ values, indicative of meteoric water origin. (For interpretation of the references to colour in this figure legend, the reader is referred to the Web version of this article.)

albeit aligned with the foliation developed within the fault zone. The fault-parallel mineralisation comprises coarse interfingering quartz (Qz) and calcite (Cc), with partial recrystallization due to the growth of finer calcite crystals. In the most extreme cases (Fig. 9g–i), foliated cataclasites develop well-sheared calcite clasts that share similarities with the brittle-ductile structures reported in Fig. 8d-l, although little evidence of banded calcite can be found. As illustrated in Fig. 10j and k, calcite-supported massive cataclasites exhibit a noticeable trend towards lower $\delta^{18}O$ values, setting them apart from the foliated counterparts, which are more within the main cluster. The matrix in these samples displays isotopic variability, ranging from a composition identical to the host rock to markedly lower $\delta^{18}O$ values. Euhedral calcite crystals from the fault core show lower $\delta^{18}O$ values. Most of these values come from the Gemmi region, although some originate from the Mondraleche Fault (Fig. 5a) or the Wildhorn Fault (reaching $\delta^{18}O$ values down to −17 ‰ in sample 38LC; Fig. 8m).

4.5. Clumped isotopes

A total of 19 samples were analysed for clumped isotope composition (Table 4; Fig. 11). Fig. 11a illustrates the $\delta^{18}O$ values vs clumped isotope temperature from three different nappes. Among those, the PBT, associated with a hydrothermal paragenesis, records temperatures reaching values up to 214 °C (sample 67LC I). Their significance is discussed in section 5.2.

In Fig. 11b, $\delta^{18}O$ and temperatures are correlated with specific textural categories, which constitute two different trends. The trend marked by a green arrow covers a wide temperature range of 55–216 °C, with a positive correlation between temperature and the calculated $\delta^{18}O$ of the fluid. Despite the limited number of measurements, the trend

Table 4
Primary clumped isotope values from the Rawil Depression and modelled clumped isotope temperatures are provided. The latter are computed using models based on codes of different authors (see methods 3.5 for details). PBT= Pennine Basal Thrust. * Requires the sample to be dolomite, ** partial recrystallization during exhumation from about 200 °C (pure reordering predicts 101 °C (HH21) to 140 °C as clumped isotope temperature), *** Model available only for shear heating and deformation age of less than 10 Ma, ****would necessitate shear heating.

Sample ID	Microfabric	replicates	$\delta^{18}O$ VSMOW	$\delta^{13}C$ VPDB	Calculated Temp $T\Delta_{47}$ (°C)	Calculated Temp error (°C)	HH21 (°C)	SE 15 (°C)	Hea14 (°C)
Sion-Courmayeur Zone - Pennine Basal Thrust									
67LC I	Foliation parallel vein	10	10.72	−7.85	214.4	−17/+19	250–300	*	*
67LC IV	Small vein	9	8.68	1.38	203.0	−10/+10	250–300	*	*
Helvetic nappes - Wildhorn Nappe									
24 I LC	Host rock (clast)	8	19.09	2.54	201.6	−11/+11	224–208	202	202
RF1	Veined host rock	9	13.68	1.36	162.9	−8/+8	**	**	**
RF2 I	Calcite clast	8	8.87	1.75	121.1	−10/+11	122	126	123
RF2 II	Fine cataclasite	9	11.05	1.51	122.3	−13/+15	123	127	124
RF3 I	Fine cataclasite	10	3.80	1.39	82.1	−9/+9	82.1	82.1	82.1
RF3 II	Slickenfibres	6	1.16	1.38	59.1	−7/+7	59.1	59.1	59.1
RF4 I	Matrix (yellow)	7	9.03	0.89	102.1	−7/+8	102.1	102.1	102.1
RF4 II	Calcite clast	8	11.45	1.67	130.8	−7/+7	130.8	145.0	145.0
RF5	Matrix (yellow)	8	1.20	0.21	55.5	−4/+4	55.5	55.5	55.5
RF7	Cataclasised shear band	8	9.09	1.61	109.0	−4/+5	109.0	109.0	109.0
113LC II	Mylonitic Shear band	10	17.77	2.00	216.1	−21/+24	249–241	***	***
114aLC I	Matrix (dark)	9	−1.18		125.6	−9/+10	125.6	132.0	130.0
114aLC II	Cataclasised mylonite clast	9	10.05	2.10	157.1	−7/+7	164–165	192	****
130LC	Fault-parallel mineralisation	8	−5.54	2.19	85.2	−3/+3	85.2	85.2	85.2
Helvetic nappes - Doldenhorn Nappe									
125LC II	Calcite clast	10	−11.02	0.64	133.2	−6/+7	134	140	138
126LC	Fine cataclasite	10	−10.08	0.48	112.0	−11/+12	112	112	112
129LC	Sparry aggregate	9	−1.78	0.97	182.7	−10/+10		240–183	200–183

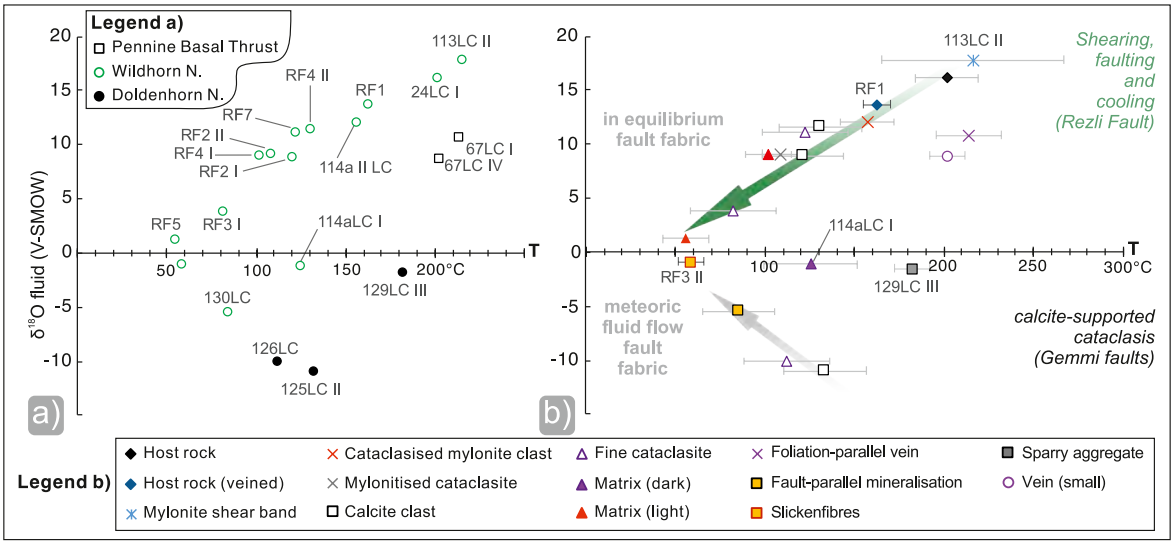

Fig. 11. a) $\delta^{18}O$ vs $\delta^{13}C$ SMOW clumped-isotope temperature plots categorised by nappes. b) plots of clumped isotopes keyed by structural type. For clarity errors are only plotted in b). Temperature trends, representing in equilibrium (mainly from the Rezli Fault), transitional and meteoric influences on faulting.

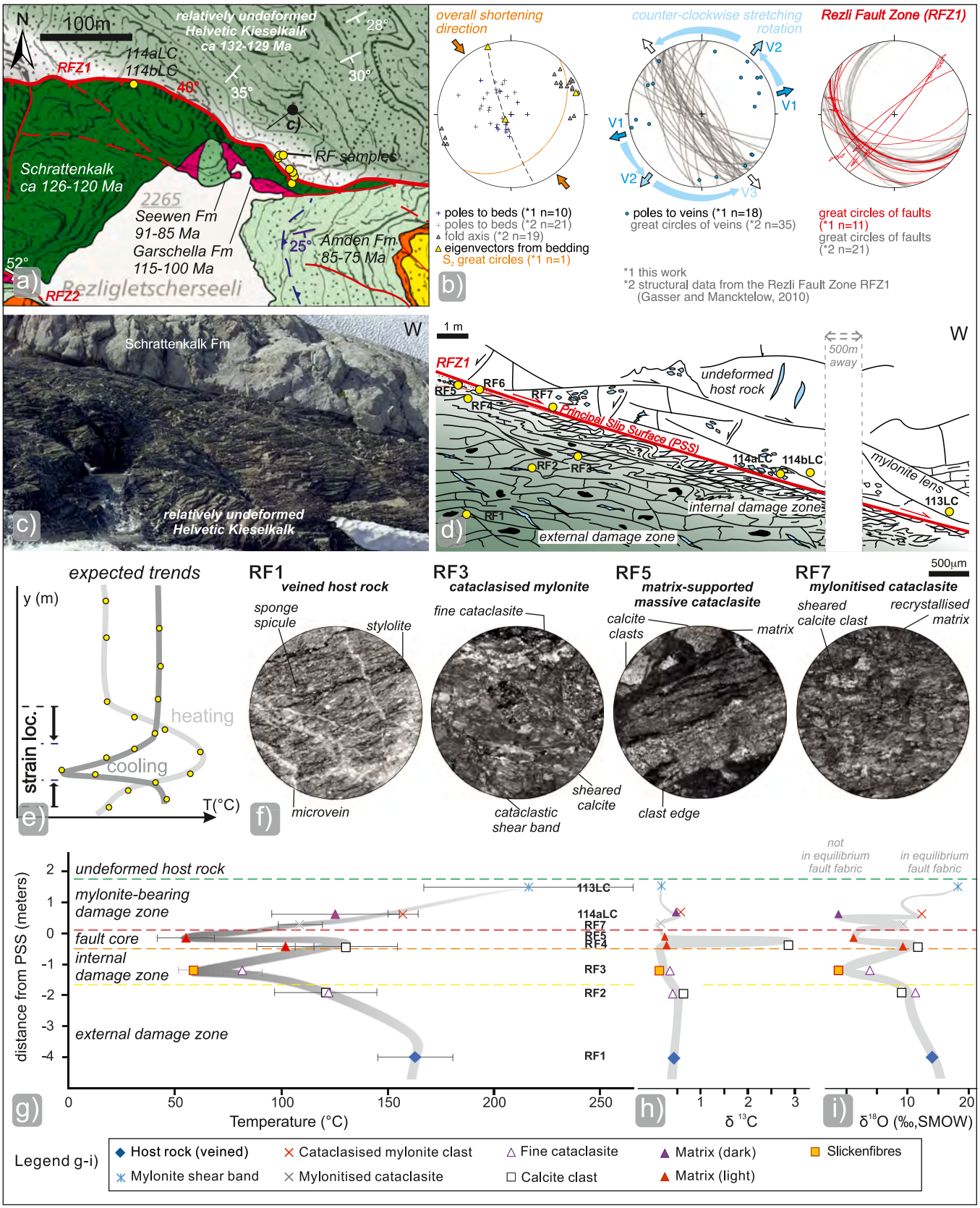

Fig. 12. Rezli Fault Zone. a) detailed tectonic map of the sampling area (modified after Gasser and Mancktelow, 2010). b) stereoplots of local structural elements of the northern branch of the sampled fault zone (RFZ1 in c). d) structural sketch and sampling across the principal slip surface, e) together with expected cooling/heating trends; f) microstructures; g) clumped isotopes plotted against distance to the principal slip surface. h) variations in $\delta^{13}C$ and i) $\delta^{18}O$ across the Rezli Fault keyed by the same structural type as in e).

marked by a grey arrow demonstrates instead a clear negative correlation, with higher temperatures associated with more negative $\delta^{18}O$ values of the fluids percolating in the Wildhorn (130LC) and Doldenhorn Nappes (126LC, 125LC; see also Fig. 10j). For positive $\delta^{18}O$ values (Fig. 11b), we identified a trend that can be considered to be in equilibrium with the host rock values (green arrow), while another trend shows progressively more negative values (grey arrow). The green arrow trend is associated with fault fabrics, primarily related to the Rezli Fault (Fig. 5), connecting the rock-buffered mylonites (T = 160–220 °C) with the cataclasites (T = 60–80 °C) (Fig. 11b). Only one host rock sample (24LC; see also Fig. 6k-l) and one veined host rock sample (RF1) were measured, giving temperatures of 202 ± 11 °C and 162.9 ± 8 °C, respectively. Samples that yield calculated negative $\delta^{18}O_{fluid}$ values show temperatures from 80 to 150 °C, and are linked to microstructural types like sparry aggregates and fault-parallel mineralisations from the NW-striking post-nappe calcite-supported massive cataclasites of faults cross-cutting the Doldenhorn Nappe at Gemmi (Fig. 5). Negative $\delta^{18}O_{fluid}$ compositions are also calculated for mineralisations related to calcite-supported foliated cataclasites, which record temperatures of ca. 85 ± 3 °C; (sample 130LC; see also Fig. 10j), showing the influx of meteoric fluids also in sheared rocks.

Detailed sampling along the Rezli Fault (Fig. 12a) provided temperature trends across a brittle-ductile fault zone that, according to Gasser and Mancktelow (2010), is subdivided into two main fault zones. A summary of the structural elements from published and new data is presented in Fig. 12b, along with the structural interpretation of the sampled area at the northernmost branch of the Rezli Fault (RFZ1; Fig. 12c and d). The purpose of this detailed sampling was to obtain information on possible effects of shear heating or of cooling embrittlement of the fault (Fig. 12e), which is microstructurally described by the brittle-ductile fabric in Fig. 12f. While the veined rocks (sample RF1) are mostly dominated by microveining and stylolites, the brittle-ductile rocks display either clasts of shear banded calcite wrapped by fine cataclasite/matrix (RF3, RF5), or sheared calcite clasts within a recrystallized matrix (RF7). More microstructures from this sampling area are shown in Fig. 8j-l and 9j-i. As shown in Fig. 12g, we observe a stepwise temperature drop of about 150 °C towards the fault core. When we consider the $\delta^{18}O$ from calculated fluids, we observe that colder temperatures are associated with brittle structures such as slickenfibres on a minor slip surface (RF3) or the matrix of the principal slip surface (RF5). In the fault core, values vary depending on the texture. Across the section, in the mylonite lens preserved within the brittle damage zone (Fig. 8a–c), relatively low $\delta^{18}O$ values were found, for example in the dark matrix (114aLC II; see Fig. 9k) or in other intervening brittle structures (e.g., RF3; Fig. 12g).

5. Discussion

5.1. Thermochronologic insights into the regional thermal evolution

The available thermochronologic dataset (including ZFT, ZHe, AFT and AHe from this and previous studies; Tables 2, 3, Table S1), show that ZFT ages younger than the Alpine metamorphism (i.e., partially to fully reset) are only found within the backlimb region (Rahn, 2001), which is characterised by metamorphic conditions of uppermost diagenetic to lowermost greenschist facies (Fig. 1a). Reset ZHe ages are confined to the axial and backlimb regions. The youngest AFT are found within the ECMs (Fig. 1c), while ages closer to or within the Rawil Depression are relatively older. As shown in Fig. 1d, AFT and AHe ages decrease towards the southeast.

Applying a geothermal gradient of 27 °C/km (Ziegler and Isler, 2013), exhumation, from late Oligocene to Middle Miocene, occurred at a rate of ~0.14 km/Myr in the most depressed area (Ultrahelvetic nappes, Plaine Morte; Fig. 4a and 5a), and of ~0.22 km/Myr on the eastern side (Gemmi Pass; Fig. 4c and 5a). In the Late Miocene, rates surged to ~0.65 km/Myr at Plaine Morte, while on the eastern side they reached ~0.86 km/Myr, marking the shift from the early to the late stage of exhumation. This rate significantly increased between 9.7 Ma (early Tortonian) and 3.8 Ma (Early Pliocene) on the eastern side, whereas Plaine Morte accelerates only to 0.35 km/Myr around 7.8 Ma in the uppermost Tortonian. Exhumation rates in the eastern side decreased to values of ~0.23 km/Myr over the last 3.8 Myr, suggesting the Rawil Depression has not been prominently forming since then. In the backlimb region, exhumation rates accelerated from ~0.44 km/Myr during the Tortonian-Early Pliocene period to ~1 km/Myr in recent times.

In support of these estimates, we recall that on the eastern side of the Rawil Depression, sample 128aLC (Doldenhorn Nappe, Fig. 1c, 4c and 5a) probably shows a fully reset ZHe age (although only one grain could be dated) of 18 Ma. For the modelling (Fig. 4c), this sample was combined with sample MR P 488 (AFT age of 7.3 ± 1.0 Ma) and confirms an increase of exhumation rate during the Late Miocene-Early Pliocene of about 0.86 km/Myr, followed by a slow down to 0.23 km/Myr. Because the increased exhumation rate of all modelled nappes started at around 11 Ma (Tortonian), we suggest that this corresponds to the initiation of the development of the Rawil Depression (Fig. 4). The relatively young uplift of the ECM domes near Brig and Martigny (Fig. 13) most likely deepened the depression between them (Herwegh et al., 2020). Exhumation in the backlimb region was greater than that of the region south of the Rhône Valley (Vernon et al., 2008). The already existing antiformal dome in the axial region was uplifted in the footwall of the Simplon-Rhône Fault, similar to the Aar Massif further to the east (Reinecker et al., 2008; Cardello et al., 2016).

5.2. Integrating thermochronologic, stable isotope and microstructural analyses

Incorporating modelled burial-exhumation trajectories (Fig. 4) and modelled clumped isotope formation temperatures (T_{mf}), derived from calculated temperatures ($T\Delta_{47}$) (Table 4) obtained from carefully selected microfabrics in isotopic equilibrium with the host rock, we are able to establish time-temperature constraints on the deformation experienced by the carbonates during exhumation (Fig. 13). By projecting the T_{mf} of each selected microfabric onto the exhumation trajectory of the nappe, we try to indirectly constrain the timing of its formation. Our modelling efforts concentrate on microstructures developed within fault zones or veins. We exclusively consider microfabrics with a clumped isotope signature that is primarily affected by carbonate deformation linked to the exhumation process, either because they newly formed during exhumation or because their sedimentary, diagenetic and burial history has been overprinted due to recrystallization. Further, we only include samples that show an isotopic signature that is consistent with mineralisation from a rock-buffered fluid, as was already recognized by Burkhard and Kerrich (1988). Their formation conditions can be considered in equilibrium with the surrounding host rock and thus should fall onto the burial-exhumation trajectory of the nappe.

For samples with calculated clumped isotope temperatures below approximately 130 °C, we find that all solid-state reordering models predict negligible reordering ($T_{mf} \sim T\Delta_{47}$). Thus, for samples in this temperature range $T\Delta_{47}$ can be used directly for this approach (without the necessity of modelling solid-state bond reordering).

In the following, we present case studies related to compressive (section 5.2.1) and transtensive (sections 5.2.2 and 5.2.3) deformation in carbonates.

5.2.1. The Sion-Courmayeur Zone (SCZ) and the Pennine Basal Thrust (PBT)

A PBT sigmoid from the base of the SCZ (sample 67LC; Fig. 7), that formed during the $D_{3\text{-}4}$ phases (23-19 Ma; Cardello et al., 2019, Fig. 13a) yields a $T\Delta_{47}$ of 214 ± 18 °C. T_{mf} are between ~300 °C (at 23 Ma) and ~250 °C (at 19 Ma) and modelled reordered temperatures (T_{mr}) are in the range of ~180-135 °C. This case is unique in that, within the given

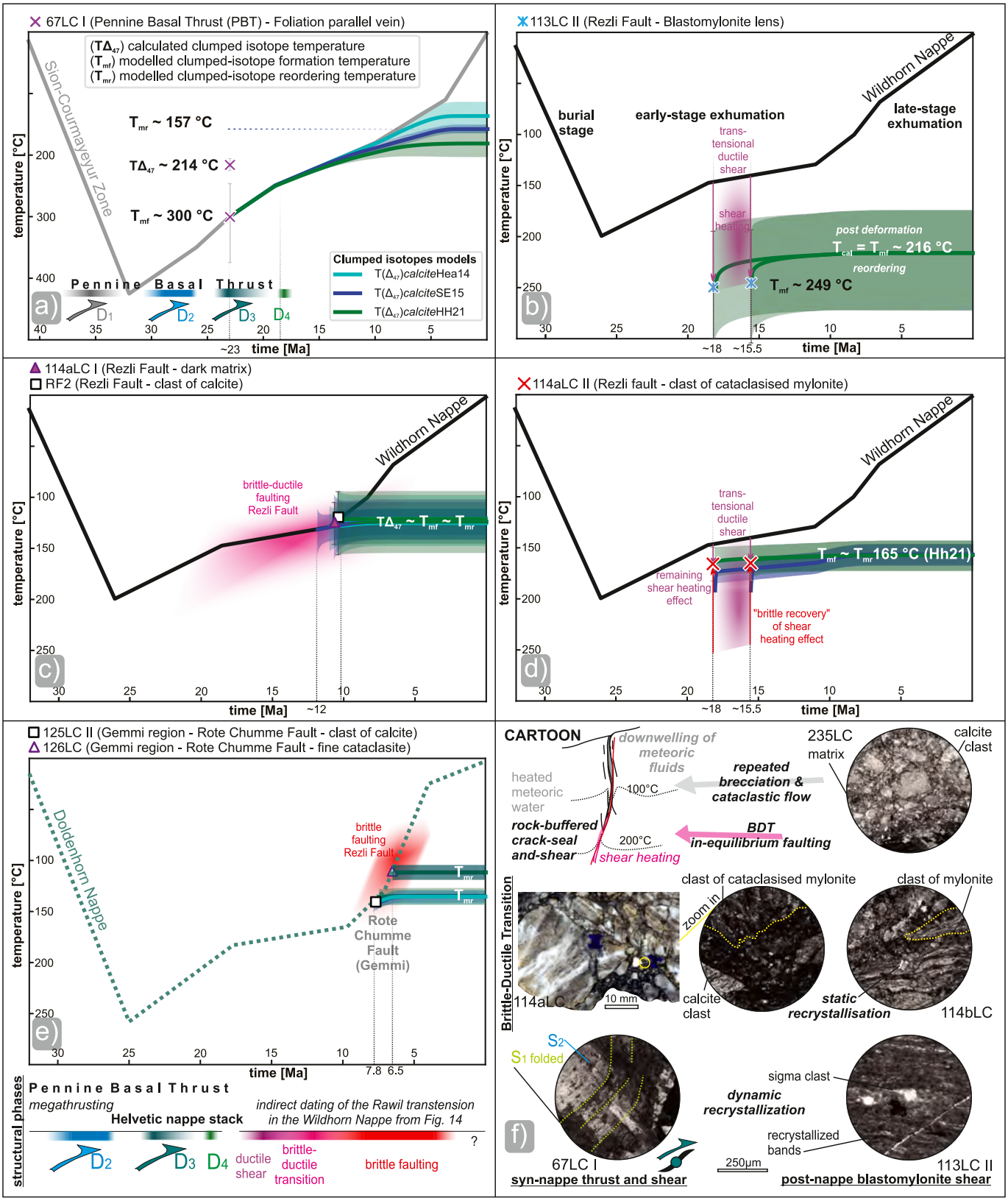

Fig. 13. a-e) Diagram illustrating examples of calculated vs. modelled clumped isotope temperatures from different nappes (for method, see text in section 3.5, explanation in section 5.2). f) Scheme of deformational processes (in bold italics) associated with their sketched geological context accompanied by optical microscopy examples.

constraints, no model can reproduce T_{cal}. This suggests that all current reordering models overestimate reordering during cooling. Of all tested models, the HH21 model performs best and it is also the only one that reproduces T_{cal}.

The predicted formation temperature T_{mp} of the PBT sigmoid is lower than that of the radiometrically constrained D_1 white-micas, which were involved in the thrusting and reached temperatures of ~350 °C (Cardello et al., 2019). The hydrothermal paragenesis associated with sample 67LC I is the result of mineralisation parallel to S_2 during SCZ exhumation (Fig. 13), potentially resulting in $\delta^{18}O$ values that are consistent with a relatively open fluid system, as observed in Figs. 7 and 11.

5.2.2. The Rezli Fault

The maximum age of the initiation of transtensional ductile shearing in the Rezli Fault is constrained by the timing of thrusting within the Wildhorn Nappe, which fades out at around 18–15.5 Ma, based on radiometric constraints on the age of thrusting from Kirschner et al. (2003).

With these constraints, a well-preserved rock-buffered calcitic blastomylonite from the Rezli shear zone (sample 113 LC; Fig. 8a–c; 12) with a $T\Delta_{47}$ of 216 ± 22 °C (Fig. 8c; 14 b) yields a T_{mf} of 246 ± 42 °C. During this period, which represents a maximum age for the development of ductile shear, the thermal stage of the Wildhorn Nappe was approximately 50–150 °C colder than the T_{mf} (and 50–85 °C colder than the $T\Delta_{47}$) recorded by the mylonite during the early stage of exhumation. While this temperature range remains ill constrained, both $T\Delta_{47}$ and T_{mf} significantly exceed the ambient temperature of the host rock at that time, as well as the modelled metamorphic peak temperature of the nappe (T < 200 °C; Fig. 13), strongly suggesting that shear heating could have played a role in the mylonitisation process (e.g. Duretz et al., 2015, Fig. 13b).

As demonstrated by the invariance of C and O isotopic composition across the fault zone (Fig. 11; Fig. 12h and i), deformation has occurred under in-equilibrium conditions, excluding significant lateral variations across the transect. In samples affected by brittle-ductile faulting, shear heating appears to be less prominent (Fig. 13c and d). A cataclasised mylonitic clast from the Rezli shear zone (sample 114aLC II; Fig. 13d), records a temperature excursion of only about 10–30 °C above ambient temperature of the Wildhorn Nappe. We interpret this as a "brittle recovery" of the shear heating effect (red arrows in Fig. 13d), whereby this clast was partially recrystallized as it was cataclasised. This is why it records a temperature that reflects a mixture between the temperature of mylonitisation (with shear heating) and that of cataclasis at lower temperatures.

5.2.3. Faults from the Gemmi region

The cataclasites from the Gemmi region originate from two distinct fault systems: the Rote Chumme Fault (sample 125LC and 126LC, Fig. 14c) with $T_{mf} \sim T\Delta_{47}$ between 110 and 140 °C; and the neotectonic fault of the Gemmi Pass (sample 129LC) with a $T\Delta_{47}$ of 183 ± 11 °C. Despite the limited displacement on these faults (<150 m; Cardello and Mancktelow, 2015), which would imply limited bottom-up connectivity, the cataclasites have $\delta^{18}O$ signatures that point to meteoric water as the source for the mineralising fluid (cf. Fig. 11), which did not significantly interact with the host rocks during infiltration. The disequilibrium conditions between host rock and mineralising fluid render the cataclasites unsuitable for directly placing them on the Doldenhorn Nappe exhumation path. However, under the assumption that the mineralising fluid temperature was the same as the host rock, the formation of the cataclasites from the Rote Chumme Fault can be constrained to be ca. 8–6.5 Ma (Fig. 5a, 9a-c). Nevertheless, this age estimate predates the 2.5–0.002 Ma age range reported by Ustaszewski et al. (2007) for the Gemmi Pass Fault. Additional data would be instrumental in determining whether these faults could link brittle faulting in this area to the variations in the exhumation rate of the Doldenhorn Nappe.

5.2.4. Constraining the microstructural processes during exhumation

As summarised in Fig. 13f, several processes affect carbonates during the early stage of exhumation. The sigmoid in the PBT (Fig. 7a–c) records the effect of thrust-and-shear related to a widespread recrystallization. On the other hand, the best-preserved example of a post-nappe blastomylonite (sample 113LC; Fig. 8a–c) shows advanced dynamic recrystallization, while BDT examples (such as 114aLC and 114bLC; Fig. 8 j-l), show embrittlement, veining and associated static recrystallization. In the context of the shear heating effect attributed to the mylonitic samples from the Rezli Fault, we recognise a temperature shift similar to that found by Maino et al. (2020), who proposed that it records transient higher temperature pulses (50–90 °C), as reproduced by the simulation of coseismic slip along narrow fault planes localized within a broad cataclastic zone.

During the brittle overprint, repeated vein-and-shear and crack-and-seal events may have influenced the development of clasts in cataclasised mylonites, which are found alongside cross-cutting calcite veins. With the overprint of more brittle processes, a cataclastic matrix developed (Fig. 13b and c). While these cataclasites appear to form at $T\Delta_{47}$<130 °C, the sampled clast of cataclasised mylonite in sample 114aLC II ($T\Delta_{47}$ = 165–19/+21 °C) seems to have formed at higher temperatures. Considering the transitional nature of the BDT fabric, cataclastic mylonite appears to represent a transition from ductile to brittle behaviour possibly related to an initial low stress/low-strain-rate event, followed by subsequent cataclastic flow. Overall, as supported by our microstructural analysis (see sections 4.4 and 4.5), foliated cataclasites (Figs. 2, 9 and 10), such as RF2 and RF4, differ from transitional fabrics, such as the mylonitised cataclasites (RF7, LC114b), in terms of recrystallization. The recrystallization is dynamic in mylonitised cataclasites and rather static in purely cataclastic examples (RF5), which are more affected by pressure solution, veining, and cataclastic flow. Mylonitised cataclasite could indicate fluctuations within this transition, resulting in cataclasitic flow followed by subsequent, although transient, ductile creep. Overall, the BDT samples may have formed during interseismic creep, similar to what was found by Bullock et al. (2014) and Del Sole et al. (2023). Considering that their isotopic values indicate limited fluid circulation within the faults, it is likely that these faults experienced intermittent periods of more open circulation and infiltration of colder fluids, leading to the development of slickenfibres (RF3, Fig. 11b). This cooling scenario, evident in the internal damage zone of the Rezli Fault, may have occurred during its cyclic brittle reactivation, as discussed by Cardello and Tesei (2013; Fig. 13f). As for the calcite-supported cataclasites in the Gemmi region (Fig. 5a), given their disequilibrium isotopic signature yet relatively high estimated temperatures (Fig. 11a), it is highly likely that meteoric water infiltrated deep into a geothermal system (Fig. 13f).

5.3. Carbonate deformation of the Wildhorn Nappe rocks through the brittle-ductile transition

In Fig. 14, we graphically summarize our results and compare them with previous publications. The burial/exhumation path (Fig. 14a) chosen as representative of the in-equilibrium BDT post-nappe faulting, shows initiation of shearing at around 18-17 Ma, coinciding with the deactivation of the PBT and Wildhorn Nappe thrusting (cf. Fig. 13b) and concurrent with cooling reflected in the ZHe ages (Table 3).

Since the BDT marks the base of the seismogenic crust, its depth is contingent on various factors like thermal gradient, composition, and fluid circulation (Sibson, 1982). Considering our results, these factors are constrained across the Rezli Fault. Combining a surface temperature of ca. 2.8 °C and a geothermal gradient of 27 °C/km (Fig. 14a–Ziegler and Isler, 2013), we propose that the Wildhorn Nappe experienced burial to an approximate depth of 7.5 km. The faults dissecting the Wildhorn Nappe evolved at depths ranging from 6 to 4 km in BDT conditions and reached at least 1.5 km depth in the more brittle regime during the Late Pliocene. This depth range corresponds with the depth of

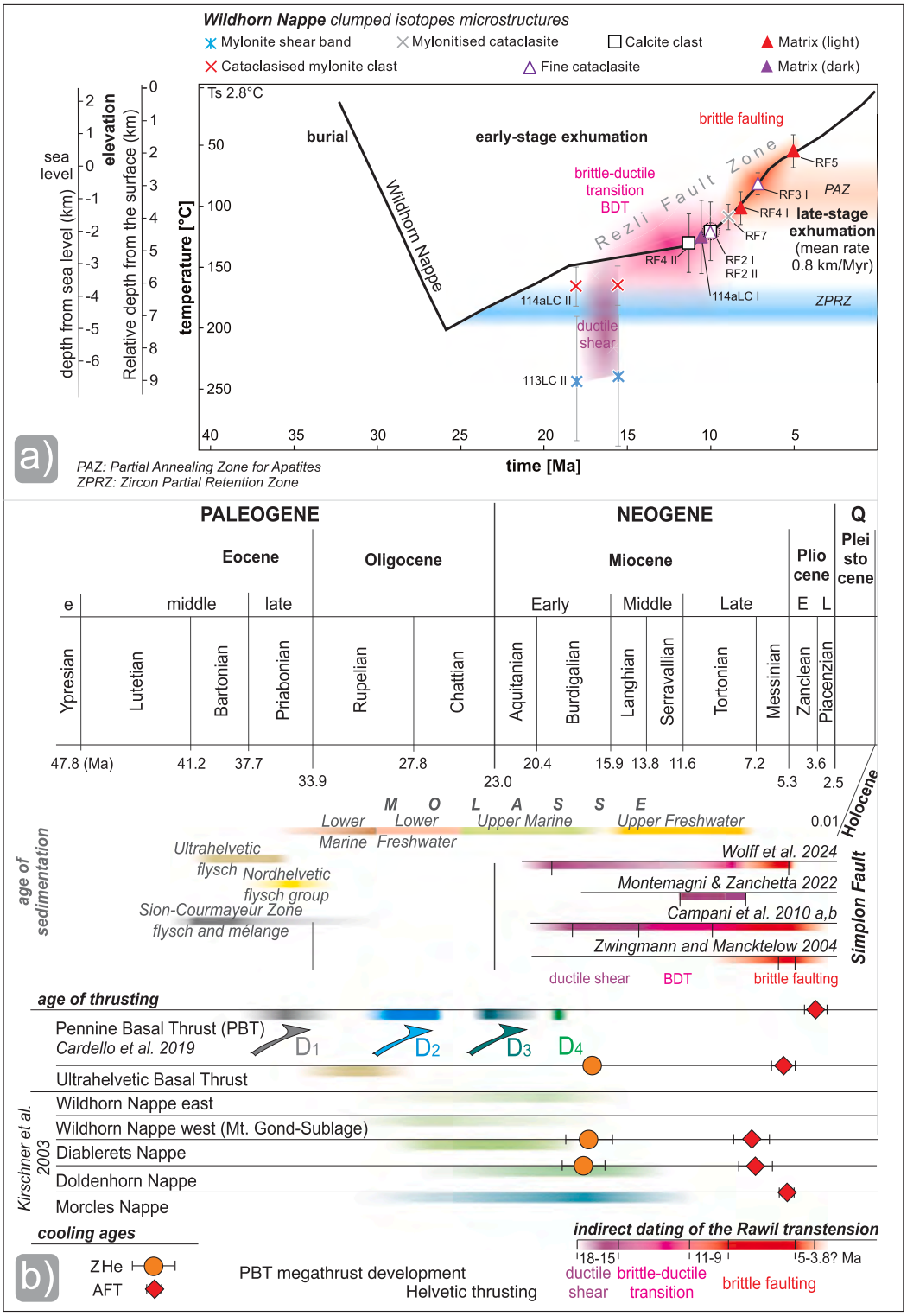

Fig. 14. a) Exhumation trajectory of the Wildhorn Nappe (bold black line, as described in section 5.2.2), encompassing temperatures, ages and relative depth. The present-day geothermal gradient is considered for T-depth conversion (cf. section 4.3). Indirect clumped isotope ages are obtained from the plot of modelled clumped isotope temperatures plotted on the exhumation segment of the Wildhorn Nappe (cf. Fig. 13). b) Chronostratigraphic regional chart comparing data from the literature and new thermochronologic results. A compilation of ages for the syn-orogenic deposits (from http://www.stratigraphie.ch) is provided along with radiometric ages from Kirschner et al. (2003), Campani et al. (2010a,b), Cardello et al. (2019), Montemagni and Zanchetta (2022), and Wolff et al. (2024). This allows indirect dating of transtension during the exhumation of the Rawil Depression, as underscored in a). Time scale limits have been rounded to the first decimal after the international chronostratigraphic chart (www.stratigraphy.org, version 2023/09).

current earthquakes below the Rawil Depression (Lee et al., 2023; Truttmann et al., 2023), located in still buried carbonates (Fig. 1c). Despite the maximal burial depth reached by the Wildhorn Nappe in the Rawil Depression, as established in section 5.2.2, blastomylonite formation suggests shear heating within the Rezli Fault zone at around 18–15.5 Ma.

The younger limit on the timing of BDT deformation is indicated by two ages from the youngest 'ductile end member', the RF7 mylonitised cataclasite, dated at about 9 Ma, and the oldest 'brittle structure' at about 11 Ma (RF4 foliated cataclasite). During the early Tortonian, the transition from the early to late stages of exhumation is reflected in the observed microstructural changes. The age of the coldest brittle microstructure, from 9 to 5 Ma (sample RF5 massive cataclasite), indicates the timing of brittle faulting along the Rezli Fault. This embrittlement is clearly related to a significantly increased exhumation rate between 9.7 Ma (early Tortonian) and 3.8 Ma (Early Pliocene) in the footwall of the Rezli Fault (see section 5.1). The early stage of exhumation was primarily governed by ductile processes involving dislocation creep and dynamic recrystallization, gradually superimposed by more distributed brittle faulting around 11 Ma until about 3.8 Ma (see section 5.1).

In Fig. 14b, the summary of the age of syn-orogenic sedimentary units of the European foreland and radiometric ages show that the transition from megathrusting (Cardello et al., 2019) to development of the nappe stack (Kirschner et al., 2003) corresponds to the onset of exhumation of the Rawil Depression. This is in line with the age of exposed BDT structures (Figs. 8 and 12) of the Rezli Fault (Fig. 14b–d; 15a). Comparing these results with those of previous studies (Fig. 14b), we notice that the end of thrusting roughly coincides with the onset of ductile shear in the Simplon Fault at around 18 Ma (Grasemann and Mancktelow, 1993; Campani et al., 2010b). The transition to brittle faulting tends to also correspond in the two areas, being at 9 Ma in the Rawil Depression and ending at about 8–10 Ma in the footwall of the Simplon Fault (Campani et al., 2010a; Montemagni and Zanchetta, 2022). On the end-of-faulting issue, Wolff et al. (2024) estimate that movement on the Simplon Fault ceased around 5.3 Ma, in broad agreement with less well constrained estimates of Grasemann and Mancktelow (1993), Zwingmann and Mancktelow (2004), and Campani et al. (2010a) of around 3–5 Ma, and consistent with our results suggesting that movement on the Rezli Fault may have ceased around 5 Ma. This end-of-faulting age estimate cannot be generalised to the entire Rawil Depression, as also indicated by 1) the post-glacial movements dated by Ustaszewski et al. (2007) and 2) by the local active seismicity, which was related to near-surface faulting by Lee et al. (2023; Fig. 1c) and Truttmann et al. (2023).

6. Conclusions

Combining new and published low-temperature thermochronology data, clumped isotopes in carbonate veins and faults, and relative age relationships from field observations and radiometric estimates constrains the T-t history and processes active during exhumation of carbonates through the brittle-ductile Transition (BDT) in the Rawil Depression.

This leads to the following conclusions.

- Exhumation rates vary over time and space. Differential exhumation rates between the structurally lowest area of the Rawil Depression (Plaine Morte) and its eastern side (Gemmi region) are about 0.1 km/Myr in the late Oligocene-Middle Miocene, and increase to 0.2 km/Myr in the Tortonian-Early Pliocene. Subsequently, differential exhumation is reversed during the last 4 Myr, with Plaine Morte exhuming faster by about 0.1 km/Myr with respect to the Gemmi region.
- Calculated clumped isotope temperatures, categorised following a new nomenclature, cover a range of macro- and micro-structural sampled lithotypes that span a temperature range from 216 °C to 55 °C.
- Formation clumped isotope temperatures are modelled using the modelled exhumation paths of the nappes that are crosscut by the post-nappe faults. In-equilibrium ductile textures from the Rezli Fault indicate localized shear heating of about 50–85 °C above the host cooling curve during mylonitisation from 18 to 15.5 Ma at least, while BDT textures formed at temperatures between ~165 °C and 150-110 °C from 15.5 to about 11–9 Ma. As exhumation progressed, BDT fault rocks underwent strain localization on discrete brittle faults, while during the Late Miocene to Pliocene exhumation acceleration, additional new brittle faults were possibly formed. These structures thus show varied temperature and depth activity, with lower clumped isotope temperatures corresponding to more recent brittle faulting, which occurred between 9 and 5 Ma (at least).

In our interpretation, the formation of the Rawil Depression is linked to the uplift of the ECMs during the Tortonian-Early Pliocene, while acceleration in backlimb exhumation is tied to the normal component of movement along the Simplon-Rhône Fault over the last 4 Myr. Three regional processes, therefore, affected the Helvetic nappe stack: i) early exhumation due to ECM exhumation towards the SW and NE, shaping the Rawil Depression; ii) late-stage exhumation, where the vertical component of the Simplon-Rhône Fault acted as a normal fault, leading to faster exhumation in the backlimb; and iii) Pleistocene glaciations deepening the valleys, as seen in AFT and AHe data sets.

Beside the regional implications, our results primarily shed light on fluid-rock interaction during exhumation of carbonates through the BDT. Among the foliated shear to fault zone examples, the initial fabric experienced partial to total obliteration related to aseismic and seismic deformation. This is due to transient pressure solution, cataclasis and cyclic crystallization, causing homogenisation of the isotopic values. The significance of clumped isotope temperature estimates, especially in understanding recrystallization effects, is highlighted, by attributing dynamic and static recrystallization as well as solid-state bond reordering to temperatures higher than 120 °C, while veining, cataclastic flow and repeated brecciation become dominant at lower temperatures.

The current study establishes the meso- and micro-structural development and related fluid-rock interaction, the thermal/exhumation history and the timing of fault activity in the Rawil Depression of SW Switzerland. It may also serve as an analogue for similar carbonate-dominated seismogenic crusts, such as the active oblique normal faults in the Apennines and the eastern Mediterranean.

CRediT authorship contribution statement

Giovanni Luca Cardello: Conceptualization, Data curation, Formal analysis, Investigation, Methodology, Software, Visualization, Writing – original draft, Writing – review & editing. **Stefano M. Bernasconi:** Conceptualization, Data curation, Formal analysis, Investigation, Methodology, Resources, Software, Validation, Writing – original draft, Writing – review & editing. **Maria Giuditta Fellin:** Data curation, Formal analysis, Methodology, Validation, Writing – original draft, Writing – review & editing. **Meinert Rahn:** Conceptualization, Data curation, Formal analysis, Investigation, Methodology, Resources, Supervision, Visualization, Writing – original draft, Writing – review & editing. **Ricarda Rosskopf:** Data curation, Formal analysis, Investigation, Methodology, Software, Writing – original draft, Writing – review & editing. **Colin Maden:** Methodology, Resources, Writing – review & editing. **Neil S. Mancktelow:** Conceptualization, Data curation, Formal analysis, Funding acquisition, Investigation, Methodology, Project administration, Resources, Supervision, Validation, Visualization, Writing – original draft, Writing – review & editing.

Declaration of competing interest

The authors declare the following financial interests/personal relationships which may be considered as potential competing interests: Giovanni Luca Cardello reports financial support was provided by ETH Zurich. Giovanni Luca Cardello reports financial support was provided by Swiss National Science Foundation. If there are other authors, they declare that they have no known competing financial interests or personal relationships that could have appeared to influence the work reported in this paper.

Data availability

All the data used are presented in the main text and Supplementary Material.

Acknowledgements

This work was supported by the Swiss National Science Foundation (project number 2-77178-11 and 200021-200977). We appreciate W. Reiners for assistance with (U–Th)/He measurements. Special thanks to Jara Schnyder and Pierluigi Cerulo for their support during sample collection, to Stewart Bishop and Madalina Jaggi for their assistance in the lab, and to the Youth Hostel of Sion for logistical help. We thank Jean-Luc Epard and Henry Masson for fruitful discussions. Special acknowledgment to Andrea Brogi, Eugenio Fazio, and an anonymous reviewer for valuable feedback that improved the manuscript.

Appendix A. Supplementary data

Supplementary data to this article can be found online at https://doi.org/10.1016/j.jsg.2024.105083.

References

Anderson, N.T., Kelson, J.R., Kele, S., Daëron, M., Bonifacie, M., Horita, J., Mackey, T.J., John, C.M., Kluge, T., Petschnig, P., Jost, A.B., Huntington, K.W., Bernasconi, S.M., Bergmann, K.D., 2021. A unified clumped isotope thermometer calibration (0.5–1,100 C) using carbonate-based standardization. Geophys. Res. Lett. 48 (7), e2020GL092069.

Berger, A., Engi, M., Erne-Schmid, S., Glotzbach, C., Spiegel, C., de Goede, R., Herwegh, M., 2020. The relation between peak metamorphic temperatures and subsequent cooling during continent–continent collision (western Central Alps, Switzerland). Swiss J. Geosci. 113 (1), 1–18.

Bernasconi, S.M., Daëron, M., Bergmann, K.D., Bonifacie, M., Meckler, A.N., Affek, H.P., Anderson, N., Bajnai, D., Barkan, E., Beverly, E., Blamart, D., Burgener, L., Calmels, D., Chaduteau, C., Clog, M., Davidheiser-Kroll, B., Davies, A., Dux, F., Eiler, J., Elliott, B., Fetrow, Fiebig, A.C., Goldberg, S., Hermoso, M., Huntington, K. W., Hyland, E., Ingalls, M., Jaggi, M., John, Jost, C.M., B, A., Katz, S., Kelson, J., Kluge, Kocken, T., I, J., Laskar, A., Leutert, T.J., Liang, D., Lucarelli, J., Mackey, T.J., Mangenot, X., Meinicke, N., Modestou, S.E., Müller, I.A., Murray, S., Neary, A., Packard, N., Passey, B.H., Pelletier, E., Petersen, S., Piasecki, A., Schauer, A., Snell, K.E., Swart, P.K., Tripati, A., Upadhyay, D., Vennemann, T., Winkelstern, I., Yarian, D., Yoshida, N., Zhang, N., Ziegler, M., 2021. InterCarb: a community effort to improve interlaboratory standardization of the carbonate clumped isotope thermometer using carbonate standards. G-cubed 22 (5), e2020GC009588.

Bernoulli, D., Jenkyns, H.C., 1974. Alpine Mediterranean and central Atlantic Mesozoic facies in relation to the early evolution of the Tethys. In: Book: Modern and Ancient Geosynclinal Sedimentation. Special Publications of SEPM. https://doi.org/10.2110/pec.74.19.0129.

Berio, L.R., Mittempergher, S., Storti, F., Bernasconi, S.M., Cipriani, A., Lugli, F., Balsamo, F., 2022. Open–closed–open palaeofluid system conditions recorded in the tectonic vein networks of the Parmelan anticline (Bornes Massif, France). J. Geol. Soc. 179 (5), jgs2021–j2117.

Boutoux, A., Bellahsen, N., Nanni, U., Pik, R., Verlaguet, A., Rolland, Y., Lacombe, O., 2016. Thermal and structural evolution of the external Western Alps: Insights from (U–Th–Sm)/He thermochronology and RSCM thermometry in the Aiguilles Rouges/Mont Blanc massifs. Tectonophysics 683, 109–123. https://doi.org/10.1016/j.tecto.2016.06.010.

Brogi, A., 2006. Evolution, formation mechanism and kinematics of a contractional shallow shear zone within sedimentary rocks of the Northern Apennines (Italy). Eclogae Geol. Helv. 99, 29–47.

Bullock, R.J., De Paola, N., Holdsworth, R.E., Trabucho-Alexandre, J., 2014. Lithological controls on the deformation mechanisms operating within carbonate-hosted faults during the seismic cycle. J. Struct. Geol. 58, 22–42.

Burkhard, M., 1990. Ductile deformation mechanisms in micritic limestones naturally deformed at low temperatures (150–350 C). Geol. Soc., London, Special Publ. 54 (1), 241–257.

Burkhard, M., 1993. Calcite twins, their geometry, appearance and significance as stress-strain markers and indicators of tectonic regime: a review. J. Struct. Geol. 15 (3–5), 351–368.

Burkhard, M., Kerrich, R., 1988. Fluid regimes in the deformation of the Helvetic Nappes, Switzerland, as inferred from stable isotope data. Contrib. Mineral. Petrol. 99, 416–429.

Bussy, F., Epard, J.-L., 1984. Essai de zonéographie métamorphique entre les Diablerets et le massif de l'Aar (Suisse occidentale), basée sur l'étude des Grès de Taveyanne. Schweizerische Mineralogische und Petrographische Mitteilungen 64, 131–150.

Byerlee, J.D., 1968. Brittle-ductile transition in rocks. J. Geophys. Res. 73 (14), 4741–4750.

Campani, M., Mancktelow, N., Seward, D., Rolland, Y., Müller, W., Guerra, I., 2010a. Geochronological evidence for continuous exhumation through the ductile-brittle transition along a crustal-scale low-angle normal fault: Simplon Fault Zone, central Alps. Tectonics 29, TC3002. https://doi.org/10.1029/2009TC002582.

Campani, M., Herman, F., Mancktelow, N., 2010b. Two-and three-dimensional thermal modeling of a low-angle detachment: exhumation history of the Simplon Fault Zone, central Alps. J. Geophys. Res. Solid Earth 115 (B10).

Cardello, G.L., 2013. The Rawil depression: its structural history from cretaceous to neogene (doctoral dissertation, ETH). Diss. ETH Library N° 21176, 212, 2 maps.

Cardello, G.L., Mancktelow, N.S., 2014. Cretaceous syn-sedimentary faulting in the Wildhorn nappe (SW Switzerland). Swiss J. Geosci. 107, 223–250.

Cardello, G.L., Mancktelow, N.S., 2015. Veining and post-nappe transtensional faulting in the SW Helvetic Alps (Switzerland). Swiss J. Geosci. 108 (2), 379–400.

Cardello, G.L., Tesei, T., 2013. Transtensive faulting in carbonates at different crustal levels: examples from SW Helvetics and Central Apennines. Rendiconti online della Società Geologica Italiana 29, 20–23.

Cardello, G.L., Almqvist, B.S., Hirt, A.M., Mancktelow, N.S., 2016. Determining the timing of formation of the Rawil Depression in the Helvetic Alps by palaeomagnetic and structural methods. Geol. Soc., London, Special Publ. 425 (1), 145–168.

Cardello, G.L., Di Vincenzo, G., Giorgetti, G., Zwingmann, H., Mancktelow, N., 2019. Initiation and development of the Pennine Basal Thrust (Swiss Alps): a structural and geochronological study of an exhumed megathrust. J. Struct. Geol. 126, 338–356.

Clemenzi, L., Storti, F., Balsamo, F., Molli, G., Ellam, R., Muchez, P., Swennen, R., 2015. Fluid pressure cycles, variations in permeability, and weakening mechanisms along low-angle normal faults: the Tellaro detachment, Italy. GSA Bulletin 127 (11–12), 1689–1710.

Coombs, D.S., Nakamura, Y., Vuagnat, M., 1976. Pumpellyite-actinolite facies schists of the Taveyanne formation near Loèche, Valais, Switzerland. Journal of Petrology 17, 440–471.

Del Sole, L., Mazzoli, S., Carafa, M.M., Toffol, G., Pennacchioni, G., Giuli, G., Invernizzi, C., Tondi, E., 2023. Interseismic creep of carbonate-hosted seismogenic normal faults: Insights from central Italy. Geol. Soc. Am. Bull. https://doi.org/10.1130/B36954.1.

Delle Piane, C., Clennell, M.B., Keller, J.V., Giwelli, A., Luzin, V., 2017. Carbonate hosted fault rocks: a review of structural and microstructural characteristic with implications for seismicity in the upper crust. J. Struct. Geol. 103, 17–36.

Dennis, K.J., Schrag, D.P., 2010. Clumped isotope thermometry of carbonatites as an indicator of diagenetic alteration. Geochem. Cosmochim. Acta 74 (14), 4110–4122.

Dietrich, D., 1989. Fold-axis parallel extension in an arcuate fold-and thrust belt: the case of the Helvetic nappes. Tectonophysics 170 (3–4), 183–212.

Dietrich, D., McKenzie, J.A., Song, H., 1983. Origin of calcite in syntectonic veins as determined from carbon-isotope ratios. Geology 11, 547–551.

Dietrich, D., Casey, M., 1989. A new tectonic model for the Helvetic nappes. Geol. Soc., London, Special Publ. 45 (1), 47–63.

Di Toro, G., Han, R., Hirose, T., De Paola, N., Nielsen, S., Mizoguchi, K., Ferri, F., Cocco, M., Shimamoto, T., 2011. Fault lubrication during earthquakes. Nature 471 (7339), 494–498.

Doglioni, C., Carminati, E., Petricca, P., Riguzzi, F., 2015. Normal fault earthquakes or graviquakes. Sci. Rep. 5 (1), 12110.

Duretz, T., Schmalholz, S.M., Podladchikov, Y.Y., 2015. Shear heating-induced strain localization across the scales. Phil. Mag. 95, 3192–3207.

Dürr, H.H., Meybeck, M., Dürr, S.H., 2005. Lithologic composition of the Earth's continental surfaces derived from a new digital map emphasizing riverine material transfer. Global Biogeochem. Cycles 19 (4).

Ebert, A., Herwegh, M., Pfiffner, A., 2007. Cooling induced strain localization in carbonate mylonites within a large-scale shear zone (Glarus thrust, Switzerland). J. Struct. Geol. 29 (7), 1164–1184.

Escher, A., Masson, H., Steck, A., 1993. Nappe geometry in the western Swiss Alps. J. Struct. Geol. 15 (3–5), 501–509.

Fellin, M.G., Reiners, P.W., Brandon, M.T., Wüthrich, E., Balestrieri, M.L., Molli, G., 2007. Thermochronologic evidence for the exhumational history of the Alpi Apuane metamorphic core complex, northern Apennines, Italy. Tectonics 26 (6).

Fox, M., Herman, F., Willett, S.D., Schmid, S.M., 2016. The exhumation history of the European Alps inferred from linear inversion of thermochronometric data. Am. J. Sci. 316 (6), 505–541.

Frey, M., Ferreiro Mählmann, R., 1999. Alpine metamorphism of the central Alps. Schweizerische mineralogische und petrographische Mitteilungen 79 (1), 135–154.

Gasser, D., Mancktelow, N.S., 2010. Brittle faulting in the Rawil depression: field observations from the Rezli fault zones, Helvetic nappes, Western Switzerland. Swiss J. Geosci. 103, 15–32.

Girault, J.B., Bellahsen, N., Boutoux, A., Rosenberg, C.L., Nanni, U., Verlaguet, A., Beyssac, O., 2020. The 3-D thermal structure of the Helvetic nappes of the European Alps: implications for collisional processes. Tectonics 39 (3), e2018TC005334.
Gnos, E., Mullis, J., Ricchi, E., Bergemann, C.A., Janots, E., Berger, A., 2021. Episodes of fissure formation in the Alps: connecting quartz fluid inclusion, fissure monazite age, and fissure orientation data. Swiss J. Geosci. 114 (1), 14.
Grasemann, B., Mancktelow, N.S., 1993. Two-dimensional thermal modelling of normal faulting: the Simplon Fault Zone, central Alps, Switzerland. Tectonophysics 225 (3), 155–165.
Handy, M.R., Hirth, G., Bürgmann, R., 2007. Continental fault structure and rheology from the frictional-viscous transition downward. In: Handy, M.R., Hirth, G., Hovius, N. (Eds.), Tectonic Faults — Agents of Change on a Dynamic Earth. MIT Press, Cambridge, Mass, pp. 139–182.
Heim, A., 1921. Geologie der Schweiz, Band II. Tauchnitz, Leipzig.
Hemingway, J.D., 2020. Isotopylog: Open-Source Tools for Clumped Isotope Kinetic Data Analysis.
Hemingway, J.D., Henkes, G.A., 2021. A disordered kinetic model for clumped isotope bond reordering in carbonates. Earth Planet Sci. Lett. 566, 116962.
Henkes, G.A., Passey, B.H., Grossman, E.L., Shenton, B.J., Pérez-Huerta, A., Yancey, T.E., 2014. Temperature limits for preservation of primary calcite clumped isotope paleotemperatures. Geochem. Cosmochim. Acta 139, 362–382.
Herwegh, M., Pfiffner, O.A., 2005. Tectono-metamorphic evolution of a nappe stack: a case study of the Swiss Alps. Tectonophysics 404, 55–76.
Herwegh, M., Berger, A., Glotzbach, C., Wangenheim, C., Mock, S., Wehrens, P., Baumberger, R., Egli, D., Kissling, E., 2020. Late stages of continent-continent collision: timing, kinematic evolution, and exhumation of the Northern rim (Aar Massif) of the Alps. Earth Sci. Rev. 200, 102959.
Hubbard, M., Mancktelow, N.S., 1992. Lateral displacement during Neogene convergence in the western and central Alps. Geology 20 (10), 943–946.
Kahle, H.G., Geiger, A., Bürki, B., Gubler, E., Marti, U., Wirth, B., Gubler, E., Rothacher, M., Gurtner, W., Beutler, G., Bauersima, I., 1997. Recent crustal movements, geoid and density distribution: contribution from integrated satellite and terrestrial measurements. Om *Deep structure of the Swiss Alps: results of NRP*, 20, 251–259.
Ketcham, R., 2005. Forward and inverse modeling of low-temperature thermochronometry data. In: Reiners, P., Ehlers, T. (Eds.), Low Temperature Thermochronology. Reviews in Mineralogy and Geochemistry, vol. 58, pp. 275–314.
Kirschner, D.L., Cosca, M.A., Masson, H., Hunziker, J.C., 1996. Staircase $^{40}Ar/^{39}Ar$ spectra of fine-grained white mica: timing and duration of deformation and empirical constraints on argon diffusion. Geology 24 (8), 747–750.
Kirschner, D.L., Masson, H., Cosca, M.A., 2003. An 40Ar/39Ar, Rb/Sr, and stable isotope study of micas in low-grade fold-and-thrust belt: an example from the Swiss Helvetic Alps. Contrib. Mineral. Petrol. 145, 460–480.
Lee, T., Diehl, T., Kissling, E., Wiemer, S., 2023. New insights into the Rhône–Simplon fault system (Swiss Alps) from a consistent earthquake catalogue covering 35 yr. Geophys. J. Int. 232 (3), 1568–1589.
Maino, M., Casini, L., Boschi, C., Di Giulio, A., Setti, M., Seno, S., 2020. Time-dependent heat budget of a thrust from geological records and numerical experiments. J. Geophys. Res. Solid Earth 125 (3), e2019JB018940.
Manatschal, G., Chenin, P., Ghienne, J.F., Ribes, C., Masini, E., 2022. The syn-rift tectono-stratigraphic record of rifted margins (Part I): insights from the Alpine Tethys. Basin Res. 34 (1), 457–488.
Mangenot, X., Tarantola, A., Mullis, J., Girard, J.P., Le, V.H., Eiler, J.M., 2021. Geochemistry of clumped isotopologues of CH4 within fluid inclusions in Alpine tectonic quartz fissures. Earth Planet Sci. Lett. 561, 116792.
Masson, H., Herb, R., Steck, A., 1980. Helvetic Alps of Western Switzerland, the Geology of Switzerland. A Guide Book. Part B. Birkhäuserverlag, Basel, pp. 109–153.
Montemagni, C., Zanchetta, S., 2022. Constraining kinematic and temporal evolution of a normal-sense shear zone: insights into the Simplon shear zone (western Alps). J. Struct. Geol. 156, 104557.
Mullis, J., Mählmann, R.F., Wolf, M., 2017. Fluid inclusion microthermometry to calibrate vitrinite reflectance (between 50 and 270° C), illite Kübler-Index data and the diagenesis/anchizone boundary in the external part of the Central Alps. Appl. Clay Sci. 143, 307–319.
Nardini, L., Rybacki, E., Krause, M., Morales, L.F., Dresen, G., 2020. Control of the geometric arrangement of material heterogeneities on strain localization at the brittle-to-ductile transition in experimentally deformed carbonate rocks. J. Struct. Geol. 135, 104038.
Pantet, A., Epard, J.L., Masson, H., 2020. Mimicking Alpine thrusts by passive deformation of synsedimentary normal faults: a record of the Jurassic extension of the European margin (Mont Fort nappe, Pennine Alps). Swiss J. Geosci. 113 (1), 1–25.
Passelègue, F.X., Aubry, J., Nicolas, A., Fondriest, M., Deldicque, D., Schubnel, A., Di Toro, G., 2019. From fault creep to slow and fast earthquakes in carbonates. Geology 47 (8), 744–748.
Passey, B.H., Henkes, G.A., 2012. Carbonate clumped isotope bond reordering and geospeedometry. Earth Planet Sci. Lett. 351, 223–236.
Pfiffner, A.O., 1993. The structure of the Helvetic nappes and its relation to the mechanical stratigraphy. J. Struct. Geol. 15, 511–521.
Pfiffner, O.A., 2014. Geology of the Alps. John Wiley & Sons.
Piantelli, F.M., Mair, D., Berger, A., Schlunegger, F., Wiederkehr, M., Kurmann, E., Baumberger, R., Möri, A., Herwegh, M., 2022. 4D reconstruction of the Doldenhorn nappe basement system in the Aar massif: insights into late-stage continent-continent collision in the Swiss Alps. Tectonophysics 843, 229586.
Rahn, M.K.W., 2001. The metamorphic and exhumation history of the Helvetic Alps, Switzerland, as revealed by apatite and zircon fission tracks. In: Habilitation Thesis. Freiburg University, p. 140p.
Ramsay, J.G., 1989. Fold and fault geometry in the western Helvetic nappes of Switzerland and France and its implication for the evolution of the arc of the Western Alps. In: Coward, M.P., Dietrich, D., D., Park, R.G. (Eds.), Alpine Tectonics, vol. 45. Special Publication Geological Society London, pp. 33–45.
Ramsay, J.G., Casey, M., Dietrich, D., Kligfield, R., Mancktelow, N., Schmid, S., Siddans, A.W.B., Pfiffner, A.O., 1981. Strain features of the Helvetic nappes of Switzerland. In: The Geological Society of America, 94th Annual Meeting 13. Abstracts with Programs - Geological Society of America, p. 535.
Ranalli, G., Murphy, D.C., 1987. Rheological stratification of the lithosphere. Tectonophysics 132 (4), 281–295.
Reinecker, J., Danišík, M., Schmid, C., Glotzbach, C., Rahn, M., Frisch, W., Spiegel, C., 2008. Tectonic control on the late stage exhumation of the Aar Massif (Switzerland): constraints from apatite fission track and (U-Th)/He data. Tectonics 27 (6).
Reiners, P.W., Brandon, M.T., 2006. Using thermochronology to understand orogenic erosion. Annu. Rev. Earth Planet Sci. 34, 419–466.
Reiners, P.W., Ehlers, T.A., Zeitler, P.K., 2005. Past, present, and future of thermochronology. Rev. Mineral. Geochem. 58 (1), 1–18.
Schmid, T.W., Bernasconi, S.M., 2010. An automated method for 'clumped-isotope' measurements on small carbonate samples. Rapid Commun. Mass Spectrom. 24 (14), 1955–1963.
Scholz, C.H., 1988. The brittle-plastic transition and the depth of seismic faulting. Geol. Rundsch. 77, 319–328.
Seward, D., Mancktelow, N.S., 1994. Neogene kinematics of the central and western Alps: evidence from fission-track dating. Geology 22 (9), 803–806.
Shuster, D.L., Flowers, R.M., Farley, K.A., 2006. The influence of natural radiation damage on helium diffusion kinetics in apatite. Earth Planet Sci. Lett. 249 (3), 148–161.
Sibson, R.H., 1977. Fault rocks and fault mechanisms. J. Geol. Soc. 133 (3), 191–213.
Sibson, R.H., 1982. Fault zone models, heat flow, and the depth distribution of earthquakes in the continental crust of the United States. Bull. Seismol. Soc. Am. 72 (1), 151–163.
Soom, M.A., 1990. Abkühlungs- und Hebungsgeschichte der Extern Massive und der Penninischen Decken beidseits der Simplon-Rhône-Linie seit dem Oligozän: Spaltspurdatierungen an Apatit/Zircon und K-Ar Datierungen an Biotit/Muscovit (Westliche Zentralalpen). PhD Thesis, University of Berne.
Spagnuolo, E., Plümper, O., Violay, M., Cavallo, A., Di Toro, G., 2015. Fast-moving dislocations trigger flash weakening in carbonate-bearing faults during earthquakes. Sci. Rep. 5 (1), 16112.
Stampfli, G., Marcoux, J., Baud, A., 1991. Tethyan margins in space and time. Palaeogeogr. Palaeoclimatol. Palaeoecol. 87 (1–4), 373–409.
Steck, A., 1984. Structures de déformation tertiaires dans les Alpes centrales (transversale Aar-Simplon-Ossola). Eclogae Geol. Helv. 77, 55–100.
Stolper, D.A., Eiler, J.M., 2015. The kinetics of solid-state isotope-exchange reactions for clumped isotopes: a study of inorganic calcites and apatites from natural and experimental samples. Am. J. Sci. 315 (5), 363–411.
Tavani, S., Smeraglia, L., Fabbi, S., Aldega, L., Sabbatino, M., Cardello, G.L., Maresca, A., Schirripa Spagnolo, G., Kylander-Clark, A., Billi, A., Bernasconi, S.M., Carminati, E., 2023. Timing, thrusting mode, and negative inversion along the Circeo thrust, Apennines, Italy: how the accretion-to-extension transition operated during slab rollback. Tectonics, e2022TC007679.
Tesei, T., Collettini, C., Viti, C., Barchi, M.R., 2013. Fault architecture and deformation mechanisms in exhumed analogues of seismogenic carbonate-bearing thrusts. J. Struct. Geol. 55, 167–181.
Torgersen, E., Viola, G., 2014. Structural and temporal evolution of a reactivated brittle–ductile fault–Part I: fault architecture, strain localization mechanisms and deformation history. Earth Planet Sci. Lett. 407, 205–220.
Trümpy, R., 1954. La zone de Sion-Courmayeur dans le haut Val Ferret valaisan. Eclogae geologicae Helvetiae 47, 315–359.
Truttmann, S., Diehl, T., Herwegh, M., 2023. Hypocenter-based 3D imaging of active faults: method and applications in the southwestern Swiss Alps. J. Geophys. Res. Solid Earth, e2023JB026352.
Ustaszewski, M., Herwegh, M., McClymont, A.F., Pfiffner, O.A., Pickering, R., Preusser, F., 2007. Unravelling the evolution of an Alpine to post-glacially active fault in the Swiss Alps. J. Struct. Geol. 29 (12), 1943–1959.
Valla, P.G., Shuster, D.L., van der Beek, P.A., 2011. Significant increase in relief of the European Alps during mid-Pleistocene glaciations. Nat. Geosci. 4, 688–692.
Valla, P.G., van der Beek, P.A., Shuster, D.L., Braun, J., Herman, F., Tassan-Got, L., Gautheron, C., 2012. Late Neogene exhumation and relief development of the Aar and Aiguilles Rouges massifs (Swiss Alps) from low-temperature thermochronology modeling and $^{4}He/^{3}He$ thermochronometry. J. Geophys. Res.: Earth Surf. 117 (F1).
Valla, P.G., Rahn, M., Van Der Beek, P.A., Shuster, D.L., 2016. Multi-phase late-Neogene exhumation history of the Aar massif, Swiss central Alps. Terra. Nova 28, 383–393.
Vernon, A.J., van der Beek, P.A., Sinclair, H.D., Rahn, M.K., 2008. Increase in late Neogene denudation of the European Alps confirmed by analysis of a fission-track thermochronology database. Earth Planet Sci. Lett. 270, 316–329.
Vitale, S., White, J.C., Iannace, A., Mazzoli, S., 2007. Ductile strain partitioning in micritic limestones, Calabria, Italy: the roles and mechanisms of intracrystalline and intercrystalline deformation. Can. J. Earth Sci. 44 (11), 1587–1602.
Wiederer, U., Königshof, P., Feist, R., Franke, W., Doublier, M.P., 2002. Low-grade metamorphism in the Montagne Noire (S-France): conodont Alteration Index (CAI) in Palaeozoic carbonates and implications for the exhumation of a hot metamorphic core complex. Schweizerische Mineralogische und Petrographische Mitteilungen 82, 393–407.

Woodcock, N.H., Mort, K., 2008. Classification of fault breccias and related fault rocks. Geol. Mag. 145 (3), 435–440.
Wolff, R., Hölzer, K., Hetzel, R., Dunkl, I., Anczkiewicz, A.A., 2024. Late-orogenic extension ceases with waning plate convergence: the case of the Simplon normal fault (Swiss Alps). J. Struct. Geol., 105049
Ziegler, H.J., Isler, A., 2013. Lötschberg-Basistunnel: zusammenfassender geologischer Schlussbericht. Bundesamt für Landestopografie swisstopo.
Zucchi, M., 2020. Faults controlling geothermal fluid flow in low permeability rock volumes: an example from the exhumed geothermal system of eastern Elba Island (northern Tyrrhenian Sea, Italy). Geothermics 85, 101765.
Zwingmann, H., Mancktelow, N., 2004. Timing of Alpine fault gouges. Earth Planet Sci. Lett. 223 (3–4), 415–425.